Measurement 234 (2024) 114812

Contents lists available at ScienceDirect

Measurement

journal homepage: www.elsevier.com/locate/measurement

Enhancing accuracy of surface wind sensors in wind tunnel Testing: A Physics-Guided neural network calibration approach

Zixiao Wang [a], Agathoklis Giaralis [b,c,*], Steven Daniels [d], Mingzhe He [d], Alessandro Margnelli [d], Chetan Jagadeesh [c]

[a] School of Electrical, Electronic and Mechanical Engineering, University of Bristol, Bristol, UK
[b] Department of Civil and Environmental Engineering, Khalifa University, Abu Dhabi, UAE
[c] Department of Engineering, City, University of London, London, UK
[d] AKT II, London, UK

ARTICLE INFO

Keywords:
Skin friction sensors
Pedestrian wind comfort
Physics-guided neural networks
Adaptive general regression neural networks
Irwin sensor
Wind tunnel testing

ABSTRACT

Irwin's surface wind sensor is widely used in wind tunnel testing for urban and environmental aerodynamics studies. However, the conventional physics-based calibration of this sensor could result in reduced measurement accuracy in regions with low flow velocities and high turbulence intensity. To address this issue, this study proposes a novel physics-guided neural network (PGNN) calibration approach, which couples a physics-based calibration model, derived from extended Taylor series expansions of measured wind speed, with an adaptive, data-driven general regression neural network. Sensors are calibrated within the turbulent boundary layer of an empty flat plate, considering both mean and standard deviation of wind velocity measured by high-accuracy thermal anemometry. The accuracy of calibrated sensors is then assessed using a 1:400 benchmark urban model. Experimental results show significant improvement in measurement accuracy, reducing mean absolute percentage error for wind speed standard deviation from 92.3 % with the current model to 9.8 % using PGNN.

1. Introduction

Skin friction sensors, also known as wall shear stress sensors, are instruments designed to measure the tangential frictional stress resulting from the relative motion of a fluid over a body surface due to the non-slip condition [1]. These sensors play a crucial role in studying various boundary layer flow characteristics, including wall shear stress distribution, surface roughness effects, drag coefficient estimation, and flow separation [2]. By quantifying wall shear stress, they facilitate wind tunnel characterisation of wind flow patterns around buildings in urban environments relevant to pedestrian wind comfort [3,4], analysis of drag forces and surface flows on air vehicles [5,6], and investigation of various environmental phenomena such as soil erosion [7], snow drifting [8], and sediment transport [9]. In all these applications, accurate measurement of wall shear stress and shear velocity is crucial, preferably at high spatial resolution. Therefore, an ideal skin friction sensor should be omnidirectional, cost-effective, compact, and easy to use, thereby eliminating the need for precise orientation during sensor placement, enabling spatially dense deployments, and fitting within restricted areas in small-scale wind tunnel test specimens.

Depending on the application, various techniques based on different sensing principles have been developed for measuring wall shear stress. One widely used instrument for turbulent boundary layers is the Preston tube [10], whose measurement principle is based on the logarithmic law of the wall. It entails placing a Pitot tube on the wall surface facing the flow and measuring the pressure difference between the total pressure measured by the Pitot tube and the wall static pressure (through a nearby hole) on the wall. In this manner, local skin friction and shear velocity can be estimated with an accuracy typically within $\pm$ 3 % [11]. However, the Preston tube is not omnidirectional and needs to be aligned with the flow direction. More sophisticated sensors employ direct and "quasi-direct" measuring techniques such as oil-film interferometry [12], wall-implemented floating element sensors [13], and liquid crystal coating techniques [14], as well as indirect techniques such as hot-film probes [15] and micro-pillar sensors MPS^3 [1]. Indirect techniques, including the use of the Preston tube, typically rely on empirical or theoretical relationships between the measured quantity and wall shear stress, specific to certain flow conditions. A commonly

* Corresponding author at: Associate Professor, Khalifa University, Abu Dhabi, UAE.
E-mail address: agathoklis.giaralis@ku.ac.ae (A. Giaralis).

https://doi.org/10.1016/j.measurement.2024.114812
Received 14 December 2023; Received in revised form 25 April 2024; Accepted 29 April 2024
Available online 4 May 2024

used relationship involves the near-wall velocity gradient, parallel to the mean flow direction, and wall-shear stress. Comprehensive reviews on the development of skin friction sensors are available in [16,17,18]. In wind engineering, however, the adoption of these advanced sensors has been limited, arguably due to their inability to provide precise pointwise measurements, as seen with the floating element sensor [16], or due to cost and complexity, as with MPS^3 and image-based techniques [7].

Against this backdrop, Irwin [19] developed an omnidirectional surface wind sensor based on the sensing principle of the Preston tube. As illustrated in Fig. 1, this sensor features a simple configuration and can be used to measure low-frequency flow speed fluctuations (or local wall shear stress) at specific height h_s within boundary layers. Its design comprises a cylindrical hole with diameter D on the wall surface; extending from the centre of this hole is a sensor tube with an outer diameter of d, slightly smaller than D. The static pressure difference is measured between the sensor tube within the boundary layer and the base hole at the wall surface. The protruding tube, perpendicular to the wall, allows for 360-degree coverage, making the sensor practically omnidirectional and eliminating the need for careful alignment with the flow direction. Furthermore, this sensor is also compact and inexpensive to manufacture, especially with recent 3D printing technology, enabling cost-efficient simultaneous measurement at hundreds of locations and capturing flow directions from all approaching angles possible. Since its development, this sensor has found extensive application in wind tunnel studies of pedestrian-level winds [20,21] and various environmental fluid dynamics studies investigating shear-stress partitioning for vegetation canopies [22,23], as well as snow drifting on flat roof [8]. In the first application, the required Reynolds number is typically in the order of 10^5, beyond which the flow regime around the built environment is considered to be insensitive to the Reynolds number [24]. Moreover, by calibrating the wind tunnel boundary-layer to replicate the characteristics of the atmospheric boundary layer, numerous studies demonstrate the agreement between full-scale measurements and equivalent wind tunnel testing for pedestrian-level winds [25].

In terms of calibration, the conventional method involves placing this sensor within a turbulent boundary layer on a flat plate, followed by calibration across a range of flow speeds measured simultaneously by a nearby thermal anemometer at the sensor head level, h_s [19]. Importantly, the calibration duration, T, must significantly exceed the timescale of the largest turbulence eddies present in the calibration flow [19]. This requirement ensures the near-wall turbulent boundary layer reaches internal equilibrium [26], allowing for the establishment of the wall law in the region below h_s. Specifically, if the duration T is much longer than the ratio of h_s to u_τ (where u_τ represents the skin friction velocity), then there is some basis to expect that the flat-plate calibration would remain valid even for low-frequency unsteady flows, such as those encountered in pedestrian wind studies [19]. Since its introduction, the above technique is widely recognised and used in wind tunnel studies focusing on pedestrian-level wind conditions. However, empirical evidence suggests that this calibration method, alongside current physics-based calibration models [19], may not yield consistent measurement accuracy when measuring the standard deviations of flow speeds in areas with low wind speeds and high turbulence [21]. This is especially evident in scaled-down wind tunnel urban models designed for studying building-induced turbulence at pedestrian levels. In this application, accurate measurement of turbulence intensity (TI) is crucial for assessing wind comfort at critical locations within urban models. Specifically, higher TI signifies increased variations in wind speed and direction, leading to gusty and erratic wind patterns that can cause wind discomfort, walking difficulties, and even safety issues [27]. To enhance sensor accuracy, potential improvements include sensor design, manufacturing quality, and calibration strategy. Among these, calibration strategy has attracted significant research attention, as it can enhance the accuracy of existing sensors independently of the sensor design specifics and quality. In this regard, the use of classic statistical regression techniques and physics-based models for calibrating skin friction sensors has been prevalent in the literature [7,13,28,29]. Meanwhile, recent efforts have been directed towards harnessing machine learning (ML) techniques and data-driven surrogate models to optimise the placement and design of shear stress sensors [30,31]. Such ML techniques offer capabilities for modelling nonlinear and intricate correlations in complex data, for accounting for noise and uncertainties, and for reducing the reliance on knowledge of the sensor's underlying physics [32,33]. Still, ML models have not been leveraged systematically to improve the calibration of skin friction sensors.

To this end, this study introduces a PGNN calibration approach aimed at improving the accuracy of the surface wind sensor in measuring mean wind speed and speed standard deviation in regions characterised by high TI. The approach linearly combines a physics-based model, derived by extending the Taylor series expansion of the

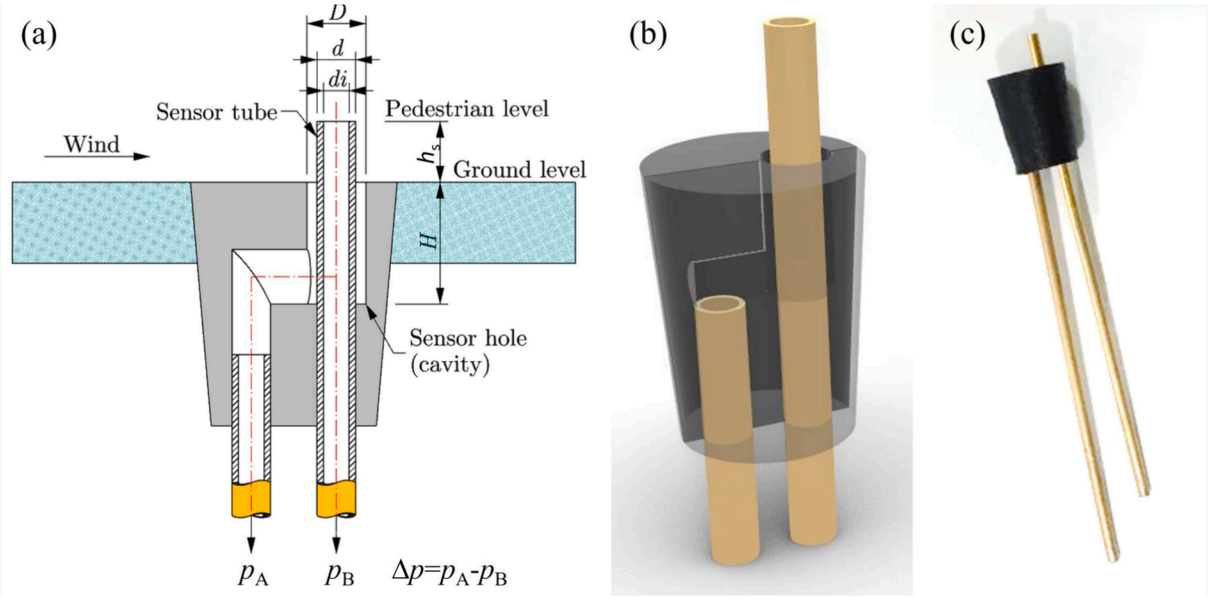

Fig. 1. Typical low-speed surface wind sensors: (a) Section diagram (principle of functionality), (b) 3D rendered view, and (c) Photo of custom-made assembled sensor with 3D-printed plastic casing and brass tubing.

instantaneous wind speed at the sensor head level, with a data-driven adaptive general regression neural network [34]. The near-wall instantaneous wind speed at a specific height within the boundary layer is expressed as a function of the differential pressure, Δp, between that height and the wall, and the Taylor series is expanded with respect to Δp. This combination leverages the GRNN's robustness against overfitting and noise, intrinsic feature selection capability, and interoperability [34,35,36]. The predictions from the two calibration models, namely the physics-based model and adaptive GRNN, are assigned weighting factors that add up to unity, which are incorporated as hyperparameters of the PGNN determined during model training. With the proposed PGNN-based approach, generic sensor calibration can be performed on an empty flat plate under idealised turbulent conditions and the calibrated sensor(s) may be used in any wind tunnel test specimen, regardless of the presence of roughness elements.

The remainder of the paper is structured as follows: in Section 2, the sensing principles and underlying physics of the surface wind sensors are reviewed, from which the physics-based calibration equations are derived. Attention is focused on demonstrating the derivation of the conventional sensor calibration equations proposed by Irwin [19] by neglecting higher-order statistical terms of the pressure difference, which compromises the sensor accuracy in turbulence characterisation. In Section 3 the proposed PGNN is introduced, discussing the underpinning theory, insights into its architecture and working principle. In Section 4, the experimental setups and measuring techniques used to generate training and testing datasets for the proposed PGNN are outlined. Section 5 reports results from a comprehensive assessment of the proposed calibration approach, and discusses input feature selection, model training, cross-validation with the physics-based calibration models and pure data-driven GRNNs, and prediction accuracy/generalisability of the model. Finally, the findings and limitations of the work are summarized in Section 6 and suggestions for future research directions are provided.

2. Omnidirectional surface wind sensors

2.1. Underlying physics

Consider a turbulent boundary layer on a smooth flat surface. In the region close to the surface, the mean wind flow velocity $\overline{u}(y)$ obeys the following universal wall law [37]

$$\frac{\overline{u}(y)}{u_\tau} = f_1\left(\frac{u_\tau y}{\nu}\right), \tag{1}$$

at a distance y from the surface, where u_τ is the skin friction velocity, ν is the kinematic viscosity of the fluid, and f_1 is a universal function independent of the local streamwise pressure gradient or flow acceleration. In Eq. (1) and henceforth, the overbar "-" is used to denote time-averaged quantities. Based on Eq. (1), it is possible to infer the mean value of flow velocity, $\overline{u}(y)$, from the skin friction velocity, u_τ, which can be, in turn, measured by a skin friction meter such as the Preston tube. The latter device makes use of a Pitot tube with a diameter d resting on the surface and pointing towards the incoming flow, and utilises the difference between the total pressure, p_{tot}, measured by the Pitot tube and the wall static pressure at a nearby location, p_s, to calculate the local skin friction velocity, u_τ, through the following relation [10]

$$\frac{(p_{\text{tot}} - p_s)d^2}{4\rho\nu^2} = f_2\left(\frac{u_\tau^2 d^2}{4\nu^2}\right), \tag{2}$$

in which ρ is the density of fluid, and f_2 is a universal function that can be established experimentally.

Based on the above principle, Irwin [19] extended Eq. (2) to relate the mean pressure difference, $\overline{\Delta p}$, between two points of an object immersed in the wall-law region to u_τ in the form of

$$\frac{\overline{\Delta p}h^2}{\rho\nu^2} = f_3\left(\frac{u_\tau h}{\nu}\right), \tag{3}$$

where h is the height of the object (or the vertical distance between the two points), and f_3 is a universal function, experimentally determined. Using Eq. (1), u_τ can be eliminated from Eq. (3), with the result being the following formula between the measured $\overline{\Delta p}$ and the mean velocity at height h,$\overline{u}(h)$

$$\frac{\overline{\Delta p}h^2}{\rho\nu^2} = f_4\left(\frac{\overline{u}(h)h}{\nu}\right), \tag{4}$$

where f_4 is a universal function.

2.2. Sensing principle and derivation of calibration equations

Based on Eq. (4), once f_4 is known, the object immersed within the turbulent boundary layer can be turned into a velocity meter by inverting Eq. (4) to infer $\overline{u}(h)$ from $\overline{\Delta p}$, which, in the case of the surface wind sensor, is the mean value of the differential pressure between the two pressure inlets in Fig. 1 (a), i.e., $\overline{\Delta p} = \overline{p_A} - \overline{p_B}$. Since the sensor in Fig. 1 is axisymmetric about a vertical axis normal to the wall surface, its calibration is the same for all azimuthal wind directions [19].

In light of Eq. (4), the following expression is provided by Irwin [19] to estimate the instantaneous wind speed at the sensor height h_s, denoted as $Q(h_s)$, in terms of the non-dimensional differential pressure, $\Delta p h_s^2/\rho\nu^2$, for $10^4 < \Delta p h_s^2/\rho\nu^2 < 10^8$

$$\frac{Q(h_s)h_s}{\nu} = 85 + 1.74\sqrt{\frac{\Delta p h_s^2}{\rho\nu^2}}, \tag{5}$$

Notably, the last equation distinguishes $Q(h_s)$ from $\overline{u}(h)$ used in Eq. (4): the former represents the mean flow speed measured by the surface wind sensor at h_s, which cannot discern the flow direction, while $\overline{u}(h)$ denotes the mean flow velocity in a consistent direction during sensor calibration. This distinction follows the conventions in Irwin [19] and Wu and Stathopoulos [21]. By noting that h_s/ν and $h_s^2/\rho\nu^2$ are constant quantities depending on the sensor's geometry, Eq. (5) can be rewritten as

$$Q(\Delta p) = A + B\sqrt{\Delta p}, \tag{6}$$

where A and B are two calibration coefficients which depend on the sensor design and dimensions. Compared to Eq. (4), the last equation establishes a means to relate the instantaneous differential pressure, Δp, and the instantaneous speed at the sensor head level, $Q(h_s)$ (see Fig. 1 (a)). From Eq. (6), it is also possible to infer the long-term mean value and standard deviation of wind speed, denoted by Q_M and Q_{SD}, respectively, from statistics of Δp. To this aim, the instantaneous speed Q in Eq. (6) is first expanded using Taylor series as

$$Q(\Delta p) = \sum_{n=0}^{\infty} \frac{Q^{(n)}(\overline{\Delta p})}{n!}(\Delta p')^n \tag{7}$$

where $\Delta p'$ is the fluctuating component of the differential pressure (i.e., $\Delta p' = \Delta p - \overline{\Delta p}$), and $Q^{(n)}(\overline{\Delta p})$ represents the n-th order derivative of the function $Q(\Delta p) = A + B\sqrt{\Delta p}$ with respect to $\Delta\rho$ evaluated at $\Delta p = \overline{\Delta p}$. By time averaging both sides of Eq. (7) and noting that $\overline{\Delta p'} = 0$, the following formula is obtained for estimating the mean wind speed

$$Q_M = \alpha + \beta\left[\sqrt{\overline{\Delta p}} + \sum_{n=1}^{m} c_n \frac{\overline{(\Delta p')^n}}{n!(\overline{\Delta p})^{n-1/2}}\right], \tag{8}$$

where $c_n = \prod_{k=1}^{n}(3/2 - k)$. By subtracting Eq. (8) from Eq. (6), the fluctuating component of the wind speed, i.e., $Q' = Q - Q_M$, can be

expressed as

$$Q' = \beta\left[\sqrt{\Delta p} - \sqrt{\overline{\Delta p}} - \sum_{n=1}^{m} c_n \frac{\overline{(\Delta p')^n}}{n!(\overline{\Delta p})^{n-1/2}}\right]. \tag{9}$$

By expanding the first term in Eq. (9) using the Taylor series followed by further algebraic manipulation, the following formula is obtained for estimating the SD wind speed

$$Q_{SD} = \beta\sqrt{\overline{\left[\sum_{n=1}^{m} c_n \frac{(\Delta p')^n - \overline{(\Delta p')^n}}{n!(\overline{\Delta p})^{n-1/2}}\right]^2}}. \tag{10}$$

As is demonstrated later in Section 5, Taylor series terms beyond the third order have negligible impact on the estimation of Q_M and Q_{SD}. Therefore, the previous expressions are truncated by setting $m = 2$ to yield two simplified formulae for estimating Q_M and Q_{SD} from Δp statistics, accounting for up to third order approximating terms, as

$$Q_M = \alpha + \beta\left[p_1 - \frac{1}{8}p_2\right], \tag{11}$$

and

$$Q_{SD} = \frac{\beta}{2}\sqrt{p_3 - \frac{1}{2}p_4 + \frac{1}{16}p_5 - \frac{1}{16}p_6}, \tag{12}$$

respectively, where

$$p_1 = \sqrt{\overline{\Delta p}},\ p_2 = \frac{\overline{(\Delta p')^2}}{\sqrt{(\overline{\Delta p})^3}},\ p_3 = \frac{\overline{(\Delta p')^2}}{\overline{\Delta p}},\ p_4 = \frac{\overline{(\Delta p')^3}}{(\overline{\Delta p})^2},\ p_5 = \frac{\overline{(\Delta p')^4}}{(\overline{\Delta p})^3},\ \text{and}\ p_6 = \frac{\left[\overline{(\Delta p')^2}\right]^2}{(\overline{\Delta p})^3}. \tag{13}$$

Notably, Eqs. (11) and (12) provide physics-based estimators of the mean value and the standard deviation of wind velocity at the sensor head level which are used in subsequent sections for sensor calibration, termed henceforth as physics-based model calibration. Additionally, it is further noted that by discarding the three higher-order polynomial terms of $\Delta\rho'$ in Eq.(13), namely p_4, p_5, and p_6, from Eqs. (11) and (12), the following estimators for the mean value and the standard deviation of wind velocity are reached

$$Q_M = \alpha + \beta\sqrt{p_1^2 - \frac{1}{4}p_3}, \tag{14}$$

and

$$Q_{SD} = \frac{\beta}{2}\sqrt{p_3}, \tag{15}$$

respectively, which are those put forward in the original work of Irwin [19] for sensor calibration. Therefore, hereafter, Eqs. (14) and (15) are termed as Irwin calibration model. The latter has been widely adopted in the literature (e.g. [21]) for the purpose at hand and is currently the conventional model used for surface wind sensor calibration.

3. Proposed physics-guided neural network (PGNN) sensor calibration approach

In the preceding section, two different models are derived for inferring the mean value of wind speed, Q_M, and the standard deviation of wind speed, Q_{SD}, by utilising statistics of Δp measurements taken by typical surface wind sensors in Fig. 1. While the model in Eqs. (11) and (12) may be more accurate than Irwin's conventional model in Eqs. (14) and (15) due to the consideration of additional terms in the expansion series in Eqs. (8) and (10), it is important to recognize that the model (Eqs. (11) and (12)) herein derived involves linear regression regardless of the number of Taylor expansion terms considered in Eqs. (8) and (10). Consequently, it cannot capture any potential nonlinear relationship between Δp statistics (a.k.a. input variables) and wind velocity mean and standard deviation (a.k.a. output variables). To address this limitation, Eqs. (11) and (12) are herein augmented by two independent data-driven models, each one assuming the form of an adaptive GRNN [34]. This augmentation results in the creation of two physics-guided GRNNs, abbreviated as PGNNs, one for Q_M estimation and one for Q_{SD} estimation based on Δp statistics measured by the wind surface sensor. The proposed PGNNs share the same network architecture shown in Fig. 2, albeit with different input features and hyperparameters for Q_M estimation and for Q_{SD} estimation. Importantly, the proposed PGNN architecture incorporates a weighting factor of γ ($0 \le \gamma \le 1$) for the physics-based predictions obtained from Eqs. (11) and (12), and a weighting factor of $(1-\gamma)$ for the data-driven predictions generated by the adaptive GRNN, as illustrated in Fig. 2. For $\gamma = 1$ the PGNN simplifies to a purely physics-based linear regressor, while for $\gamma = 0$, the PGNN becomes a data-driven nonlinear regressor.

For the GRNN component, the regression of the response/output variable, Q (which can be either Q_M or Q_{SD}), on an input variable of dimensionality m, $\mathbf{p}\in\mathbb{R}^m$ (collecting certain statistical terms of Δp), can be viewed as the computation of the most probable (expected) value of Q for each measured $\mathbf{p}$. This computation is based on a finite number of noisy measurements of $\mathbf{p}$ (using the surface wind sensor) taken by a pressure scanner, and the corresponding Q measured simultaneously with high accuracy (e.g. by a nearby thermal anemometer as will be discussed in the following section). To compute the expected value of Q for a given $\mathbf{p}$, the following conditional probability is used

$$E[Q|\boldsymbol{p}] = \frac{\int_{-\infty}^{\infty} Q f(\boldsymbol{p}, Q) dQ}{\int_{-\infty}^{\infty} f(\boldsymbol{p}, Q) dQ}, \tag{16}$$

where $f(\mathbf{p},Q)$ is the unknown joint probability density function (PDF) between the m-dimensional input vector $\mathbf{p}$ and the output Q. This PDF can be estimated from a sample of n measurements of $\mathbf{p}$ and Q using the Parzen-Rosenblatt density estimator [38,39,40]

$$\widehat{f}(\boldsymbol{p}, Q) = \frac{1}{(2\pi)^{(m+1)/2}\prod_{j=1}^{m}\sigma_j\sigma}\frac{1}{n}\sum_{i=1}^{n}\exp\left[-\sum_{j=1}^{m}\frac{(\boldsymbol{p}[j] - \boldsymbol{p}_i[j])^2}{2\sigma_j^2}\right]\cdot\exp\left[-\frac{(Q - Q_i)^2}{2\sigma^2}\right] \tag{17}$$

Importantly, this estimation method does not presuppose any specific form of the underlying PDF of the data, allowing for a wide variety of distributions to be estimated without the need to specify the form of the distribution a priori. It estimates the unknown PDF based on a sample of data points by averaging over kernel functions cantered at each measured data point [38,39,40]. In the last equation, $\mathbf{p}[j]$ denotes the j-th feature of the input variable $\mathbf{p}$, $\mathbf{p}_i[j]$ and Q_i are the j-th input feature and output variable of measurement i, respectively, and σ_j and σ are the so-called bandwidths for input dimension j and output variable (i.e., the hyperparameters subject to search), respectively. By neglecting the cross-dependence between different input dimensions, the term

$$D(\boldsymbol{p}\rightarrow\boldsymbol{p}_i) = -\sum_{j=1}^{m}\frac{(\boldsymbol{p}[j] - \boldsymbol{p}_i[j])^2}{2\sigma_j^2} \tag{18}$$

in Eq. (17) can be viewed as a reduced Mahalanobis distance between the input vector $\mathbf{p}$ and the i-th training input $\mathbf{p}_i$, denoted by $D(\mathbf{p}\rightarrow\mathbf{p}_i)$ [36]. By substituting Eqs. (17) and (18) into Eq. (16) and performing algebraic manipulation, the following estimator of the conditional probability of Q given $\mathbf{p}$ is reached

$$E[Q|\boldsymbol{p}] \approx \widehat{Q}(\boldsymbol{p}) = \frac{\sum_{i=1}^{n} Q_i \exp[D(\boldsymbol{p}\rightarrow\boldsymbol{p}_i)]}{\sum_{i=1}^{n}\exp[D(\boldsymbol{p}\rightarrow\boldsymbol{p}_i)]} \tag{19}$$

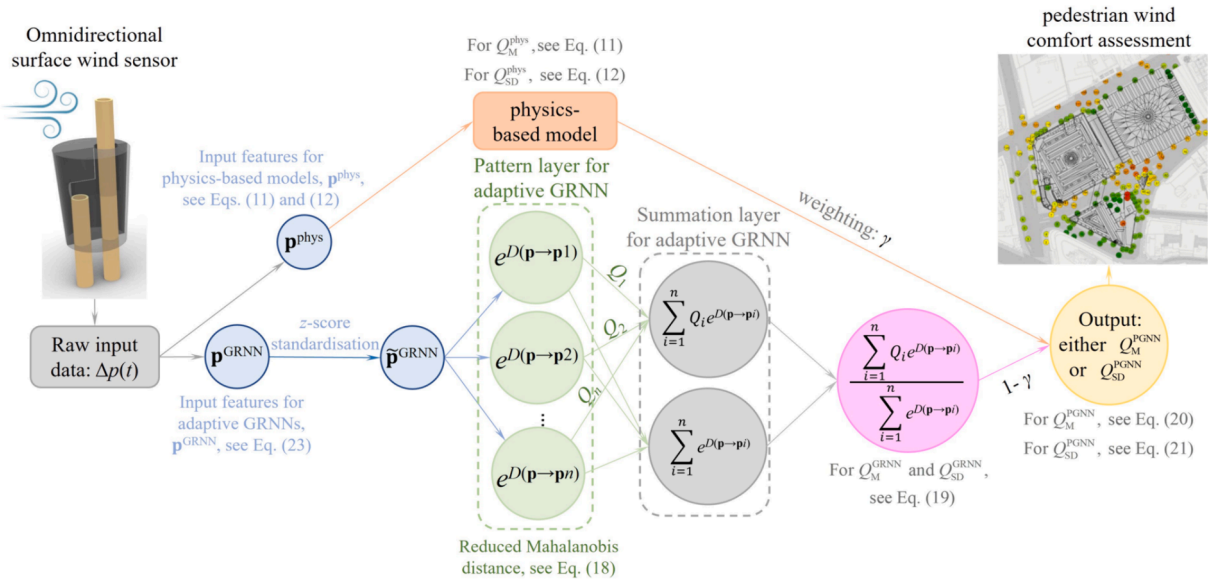

Fig. 2. Architecture of the proposed physics-guided neural network for enhancing the measurement accuracy of surface wind sensors.

The last equation facilitates an interpretation of the estimator $\widehat{Q}(\boldsymbol{p})$ as a weighted average of all measured wind velocity values, Q_i ($i = 1,\ldots, n$), where each measured Q_i is weighted exponentially according to the corresponding reduced Mahalanobis distance. Then, the adaptive GRNN model in the last equation can be used to estimate both Q_M and Q_{SD} by fitting it to the corresponding training dataset. To achieve this, Eq. (19) must be first modified so that for estimate j, i.e., $\widehat{Q}\left(\boldsymbol{p}_j\right)$, the estimate is based on inference from all other observations except the actual observed value at $\mathbf{p}_j$ [35]. This is used to prevent an artificial minimization of the error as $\boldsymbol{\sigma} = [\sigma_1,\ldots,\sigma_m]$ approaches $\mathbf{0}$, i.e., $\lim_{\sigma\to 0}\widehat{Q}\left(\boldsymbol{p}_j\right) - Q_j = 0$ At this point, Eq. (19) can be combined with models in Eqs. (11) and (12), to create two separate PGNNs as follows

$$Q_M^{PGNN}(p_1, p_2, \widetilde{\mathbf{p}}_M) = \gamma_M\left[\alpha_M + \beta_M\left(p_1 - \frac{p_2}{8}\right)\right] + (1-\gamma_M)\frac{\sum_{i=1}^{n} Q_{M,i}\exp\left[D\left(\widetilde{\mathbf{p}}_M \to \widetilde{\mathbf{p}}_{M,i}\right)\right]}{\sum_{i=1}^{n}\exp\left[D\left(\widetilde{\mathbf{p}}_M \to \widetilde{\mathbf{p}}_{M,i}\right)\right]}, \tag{20}$$

and

$$Q_{SD}^{PGNN}\left(p_3, p_4, p_5, p_6, \widetilde{\mathbf{p}}_{SD}\right) = \varepsilon_{SD} + \gamma_{SD}\left(\frac{\beta_{SD}}{2}\sqrt{p_3 - \frac{p_4}{2} + \frac{p_5}{16} - \frac{p_6}{16}}\right) + (1 - \gamma_{SD})\frac{\sum_{i=1}^{n} Q_{SD,i}\exp\left[\widetilde{\mathbf{p}}_{SD} \to \widetilde{\mathbf{p}}_{SD,i}\right]}{\sum_{i=1}^{n}\exp\left[\widetilde{\mathbf{p}}_{SD} \to \widetilde{\mathbf{p}}_{SD,i}\right]}, \tag{21}$$

for predicting Q_M and Q_{SD}, respectively. In the last equation, ε represents a disturbance variable herein introduced to account for the residuals between the actual and measured values of Q_{SD}, γ_M and $\gamma_{SD} \in [0,1]$ are the two hyperparameters that weight the relative importance of physics-based Q_M and Q_{SD} predictions in the PGNNs, respectively. Further, the input vectors $\mathbf{p}_M$ and $\mathbf{p}_{SD}$ in Eqs. (20) and (21) correspond to the input data utilised by the adaptive GRNNs for Q_M and Q_{SD} predictions, respectively. At this juncture, it is important to emphasise that in the proposed PGNN, $\mathbf{p}_M$ and $\mathbf{p}_{SD}$ may differ from those employed in Eqs. (11) and (12), potentially containing distinct sets of arbitrary statistical features of Δp (e.g., mean and SD, $\overline{\Delta p}$ and $\overline{(\Delta p')^2}$). These input features can be obtained through the intrinsic feature selection capability of the adaptive GRNN, as demonstrated in Section 5. Lastly, the symbol "~" over a variable in Eqs. (20) and (21) denotes z-score standardisation, which is employed to ensure that all input features (for the GRNN) have zero means and unity SDs. This standardisation enables faster GRNN training as well as ensures that the optimised bandwidths, $\boldsymbol{\sigma}$, for different input features have comparable magnitudes [35]. The latter is crucial for feature selection, as elaborated in Section 5.

4. Wind tunnel setups for experimental wind velocity data generation

4.1. Wind tunnel facility description

For the purposes of this study, two different wind tunnel setups are used, presented separately in the following two sub-sections: one for generating experimental data for wind sensor calibration (Section 4.2) and one for testing the accuracy of the measurements taken by the calibrated sensors (Section 4.3). Both setups make use of the industrial aerodynamics T7 wind tunnel at City, University of London [41], as shown in Fig. 3. This wind tunnel is of closed-return type with a working section of dimensions 9.0 m × 3.0 m × 1.5 m and the flow speed ranging from 4.3 m/s to 26.0 m/s. Existing boundary layer generation hardware can be used to create boundary layers representative of those over different terrains, such as open, suburban, and urban [41]. A full-width trip barrier is installed at the exit from the contraction as shown in Fig. 3 (b), which is followed by a 5 m fetch where vortex generators and roughness elements can be installed if needed. The tunnel features a round turntable with 2.4 m of diameter where specimens are installed.

4.2. Setup for obtaining sensor calibration data

To generate a representative dataset for sensor calibration, the surface wind sensor in Fig. 1 (c) is exposed to different calibration flows comprising a wide range of mean wind speeds and TIs. The sensor head, made from a brass tube with outer and inner diameters of 1.2 and 1.0 mm respectively, protrudes from a 2.6 mm circular hole and extends 3.75 mm above the sensor casing's top surface. The calibration data is obtained by installing the sensor on a flat plate device as depicted in Fig. 4 (a). The latter device is placed at the centre of the T7 turntable in Fig. 3(b). The angle of the flat plate's flap (see Fig. 4 (a)) is adjusted such that the stagnation point does not appear on the lower side the flat plate's elliptical nose to avoid flow separation. Near the leading edge of

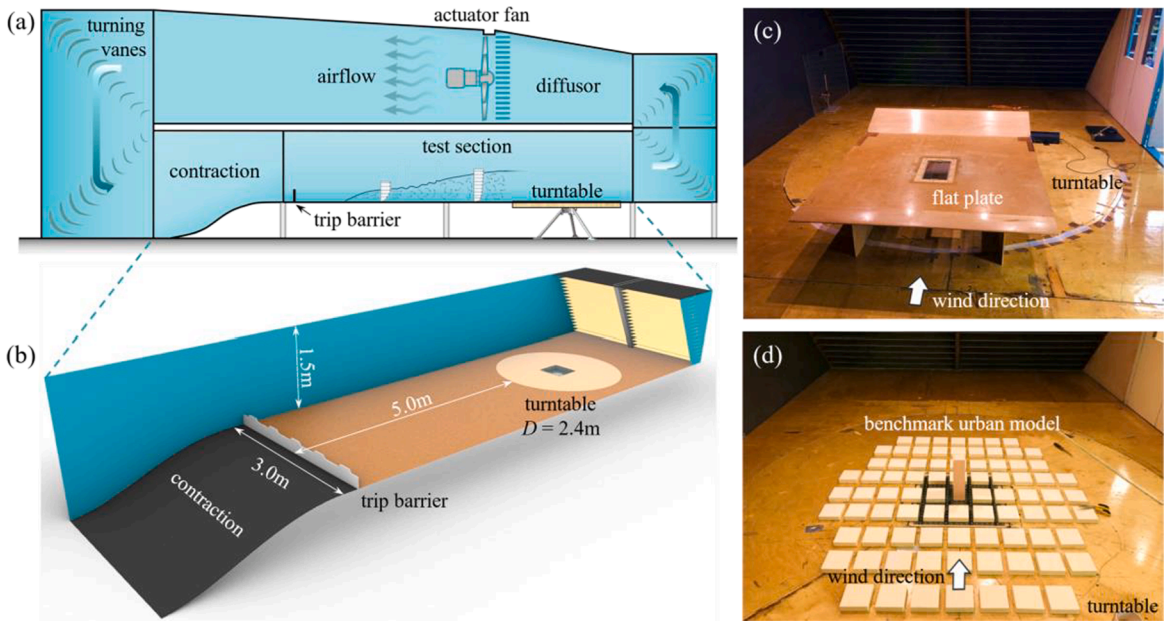

Fig. 3. (a) Side view of the industrial T7 wind tunnel at City, University of London, (b) 3D view of the wind tunnel's test section, (c) flat-plate test setup for sensor calibration, and (d) benchmark urban model setup for sensor testing.

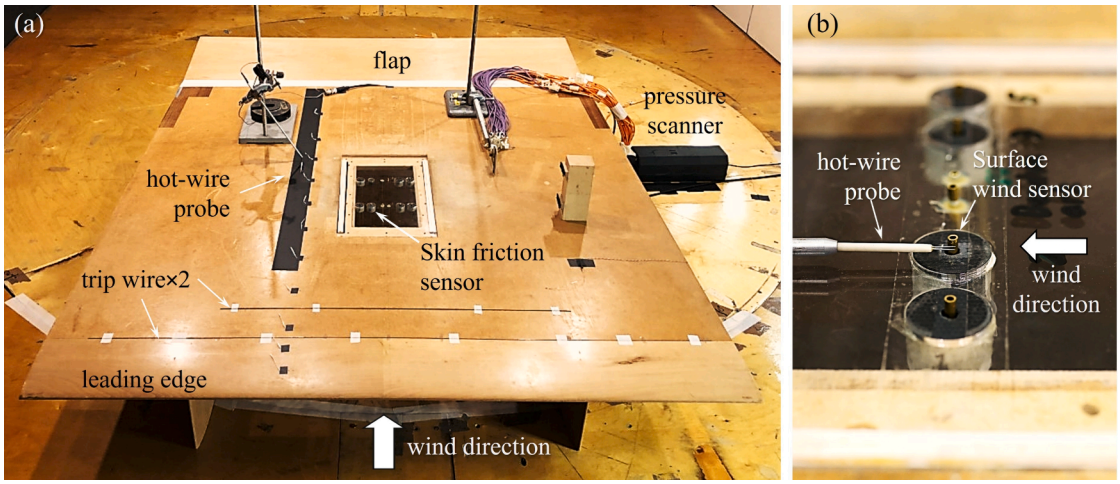

Fig. 4. (a) Flat-plate test setup, and (b) simultaneous differential pressure measurement using an surface wind sensor (being calibrated) and velocity measurement using an adjacent hot-wire probe for the calibration of the surface wind sensor.

the flat plate, two tripping wires are placed to allow for the growth of a second boundary layer on the flat plate as shown in Fig. 4 (a). To give the incoming flow different "background" TIs, six different trip barrier settings, namely, I. no barrier, II. rectangular (low), III. rectangular (high), IV. battlemented, V. castellated (low), and VI. castellated (high), are installed, one at a time, as shown in Fig. 5, on the upstream shortly after the contraction of the wind tunnel without vortex generators and roughness elements. By adjusting the inflow velocity and switching between different trip barriers, a wide range of mean wind speeds and TIs can be generated locally on the flat plate's top surface for the calibration purpose. The corresponding (normalised) mean wind speed and TI profiles at the sensor location on the flat plate are measured by a hot-wire probe from 1 mm above the top surface of the flat plate up to 50 mm and plotted in Fig. 6 (a) and (b), respectively. For comparison, the mean speed and TI profiles measured in an empty tunnel without a trip barrier and any tripping wires on the flat plate are also plotted in Fig. 6 as the baseline case. As seen, as the barrier setting changes from I to VI, the TIs at the sensor head level (i.e., at $h_s = 3.75$ mm) increases steadily, from 3.5 % in the baseline case to 31.3 % in the high castellated barrier case.

To calibrate the sensor, it is necessary to measure the flow velocity at the sensor head location, $u(h_s)$, and the differential pressure at the sensor's location between the sensor head and wall surface levels, p_A-p_B (see Fig. 1 (a)), simultaneously. To achieve this, a 1-axis hot-wire probe is positioned next to the surface wind sensor being calibrated, as illustrated in Fig. 4 (b), with a spanwise distance of 6.0 mm (approximately five times the sensor head's diameter) to minimise interference effects between the two probes, following the recommendation by Wu and Stathopoulos [21]. The hot-wire is oriented horizontally, a decision informed by the observation that, within the log-law region, wind speed across the hot-wire length typically varies under 10 % when it is oriented vertically [19]. Thus, the horizontal orientation is preferred here because the wind velocity vector on the flat plate predominantly consists of a single component along the wind direction. This orientation simplifies the alignment of the hot wire's height to the sensor head and enhances the spatial correlation in the vertical direction between the hot-wire and wind sensor measurements. The two pressure outlets of the

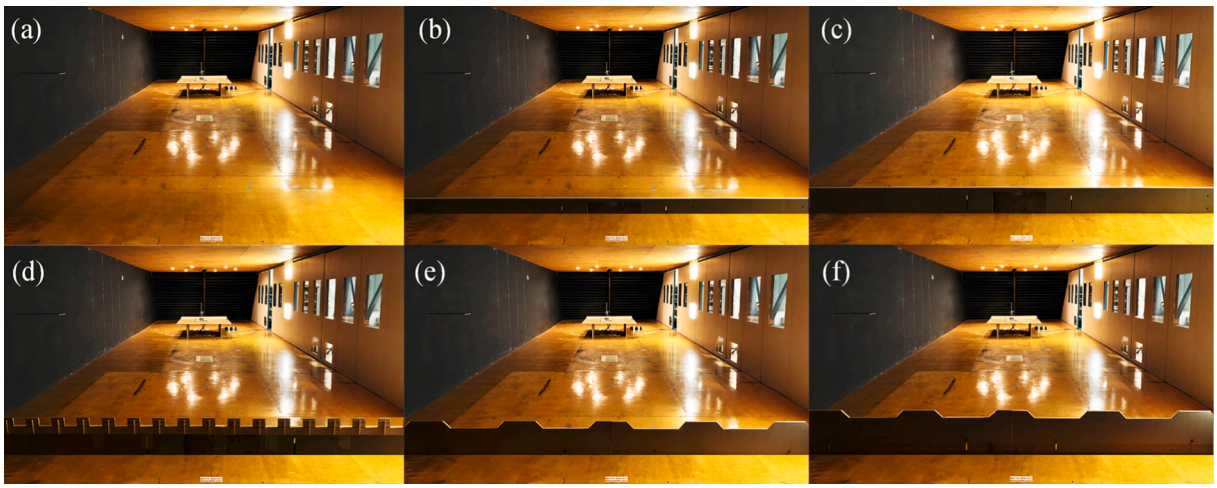

Fig. 5. Six barrier settings for simulating different mean wind speed and TI profiles on the flat plate in Fig. 3 (a): (a) No barrier, (b) Rectangular (low setting), (c) Rectangular (high setting), (d) Battlemented, (e) Castellated (low setting), and (f) Castellated (high setting).

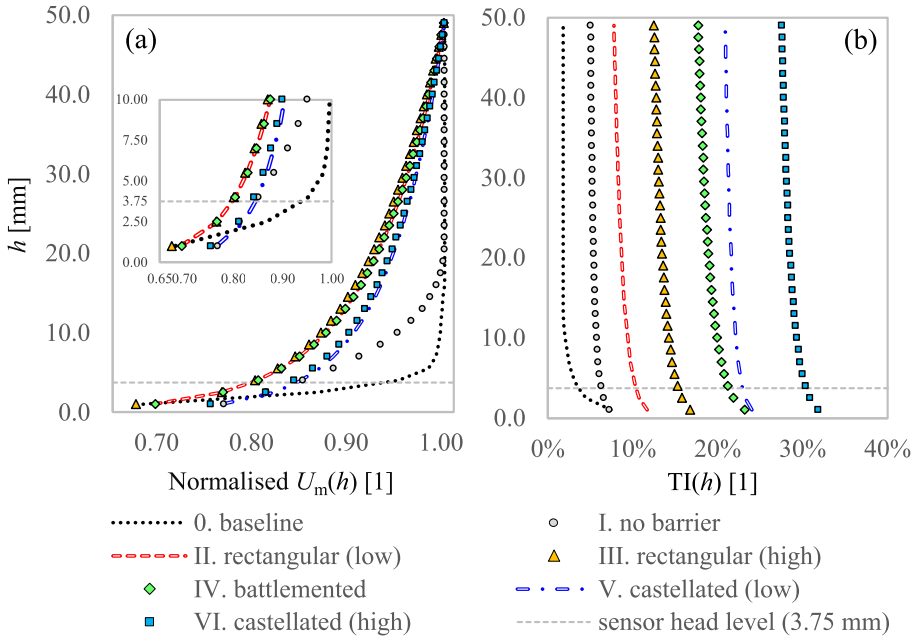

Fig. 6. (a) Normalised mean wind speed and (b) TI profiles on the flat plate in Fig. 3 (a), generated using the trip barrier settings in Fig. 5.

surface wind sensor (see Fig. 1) are connected to a 64-channel pressure scanner (with a pressure range of −0.5 to + 0.5 kPa and accuracy of ± 0.5 Pa, see [42]) to acquire the instantaneous differential pressure, while the instantaneous wind speed at the sensor head level is measured by a miniature constant temperature anemometer (CTA) [43], both at the same sampling frequency of 100 Hz. This sampling frequency is informed by the 50 Hz low-pass filtering frequency applied to both hot-wire and wind sensor data in [19]. This filtering frequency establishes the Nyquist rate in the current study, necessitating a minimum sampling frequency of 100 Hz to ensure accurate and comparable data collection. Moreover, it was observed in [19] that the sensor data generally aligns well with the hot-wire data, especially in high-speed regions, albeit with a minor phase lag attributed to the long tubing system [19]. However, this minor latency in the sensor's response time is inconsequential for the current study, as herein proposed calibration approach directly translates the long-term statistical properties of the differential pressure, Δp, into the mean and standard deviation of wind speeds. Here, "long term" refers to a duration sufficient to establish a stable mean and standard deviation. For each of the six barrier settings studied, the inflow velocity is adjusted 10 times, resulting in a range of freestream velocities at 30 cm above the flat plate's top surface between 3.4 to 9.5 m/s with a rough increment of 0.7 m/s. For barrier setting I, the measurement process is repeated for a higher freestream velocity range from 6.4 to 12.1 m/s at 10 equally spaced steps. For the above 6 barrier settings and 10 speed variations, the wind speed SDs and TIs measured by the CTA at the sensor head location are plotted against the measured mean wind speed at the same location in Fig. 7 (a) and (b), respectively, giving a total number of 70 data points (note that for setting I, there are 20 data points).

4.3. Setup for obtaining sensor accuracy assessment data

In order to create an extensive dataset for testing the proposed PGNN calibration approach, a total of 30 surface wind sensors, identical to the one illustrated in Fig. 1(c), are placed on the ground level of a benchmark urban model introduced by the Architectural Institute of Japan

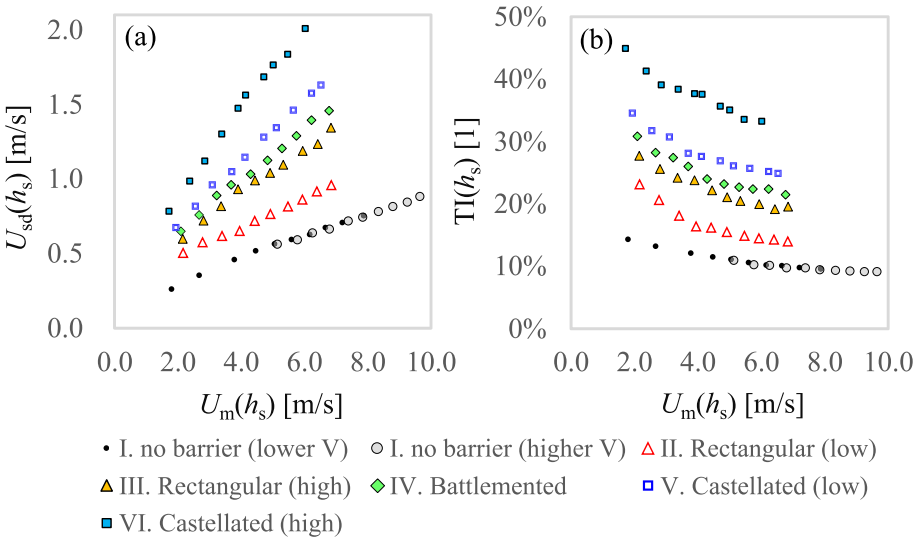

Fig. 7. Mean wind speeds vs. (a) Wind speed standard deviations, and (b) turbulence intensities at the pedestrian level, generated using the trip barrier settings in Fig. 5.

(AIJ), known as the AIJ case D. The model consists of a single high-rise block measuring 100 m in height, surrounded by simplified low-rise blocks that are 40 m by 40 m by 10 m, all at a scale of 1/400, as shown in Fig. 8(a). The urban model is installed on the turntable of the T7 wind tunnel depicted in Fig. 3(b), and the locations of the 30 probes are indicated by blue circles in Fig. 8(b). The probes are distributed on an orthogonal grid, with uniform streamwise and spanwise spacings of 2.5 cm. The inflow velocity at the end of the tunnel's contraction (refer to Fig. 3) is adjusted to ensure the mean flow velocity at the central building height ($h_{CB} = 0.25$ m) aligns with the 6.65 m/s speed used by AIJ in their initial test. The mean wind speed and TI profiles are measured 30 cm upstream from the first row of the low-rise blocks and plotted in Fig. 9(a) and (b), respectively. In Fig. 9(a), the mean wind speed profile is normalised to 1 at 300 mm rather than at the central building height. The plot reveals a nonzero streamwise velocity gradient at 300 mm, indicative of boundary layer growth, which reaches a thickness of approximately 800 mm above the tunnel floor. These profiles are generated using the castellated barrier with the high setting (i.e., setting VI from the previous section), without any additional modifiers of the boundary layer, such as vortex generators or roughness elements. The obtained profiles are comparable to those reported by AIJ in the initial test.

The 30 surface wind sensors are connected to the 64-channel pressure scanner [42] to acquire the differential pressure signal from each sensor at a sampling frequency of 100 Hz. To measure the instantaneous velocity at specific sensor locations, a miniature hot-wire probe with right-angled prongs is placed adjacent to the surface wind sensor being tested, at a transverse distance of 3.0 mm, as illustrated in Fig. 10 (a). The hot-wire probe is adjusted such that its cylindrical sensing wire is perpendicular to the tunnel floor, with the centre of the sensing wire aligned with the sensor head at $h_s = 3.75$ mm. This arrangement ensures that the horizontal velocity component of the flow at the sensor head location is always perpendicular to the sensing wire, under which condition the hot-wire probe's response is mostly insensitive to the horizontal flow direction. The use of the right-angled hot-wire probe takes advantage of the fact that, in assessing pedestrian level winds, the horizontal velocity component is generally more crucial than the vertical component, which in the case of a right-angled hot-wire probe is parallel to the sensing wire and has limited effect on the effective cooling velocity experienced by the wire, except in areas with strong downdraughts.

As in Section 4.2, simultaneous measurement of local ground level velocity (by the right-angled hot-wire probe) and differential pressure (by an adjacent surface wind sensor) is necessary to maximise spatial and temporal correlations between the two measurements. To achieve this, the hot-wire probe is moved around the AIJ case D model to

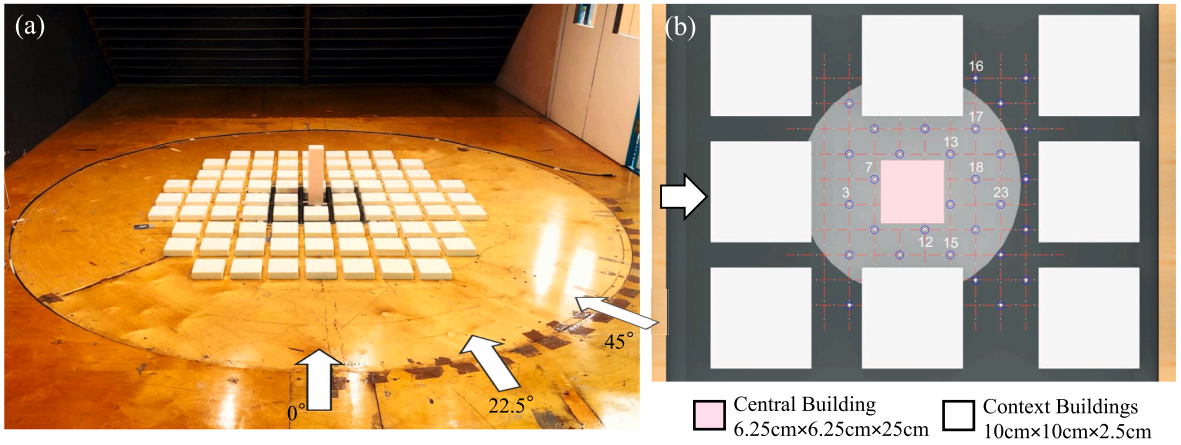

Fig. 8. (a) AIJ case D urban model setup on the turntable of the T7 wind tunnel in Fig. 3, and (b) locations of 32 surface wind sensors around the central building of the AIJ case D model and 9 probe locations chosen for surface wind sensor testing.

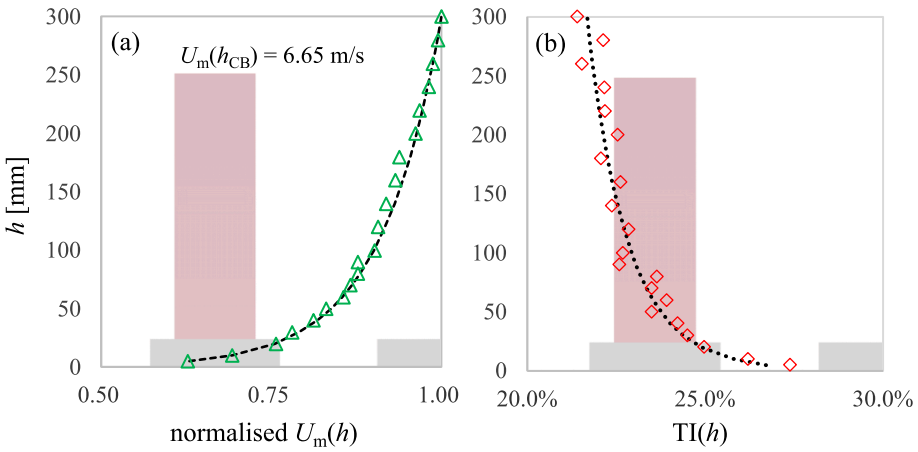

Fig. 9. (a) Normalised mean wind speed and (b) TI profiles measured at the windward edge of the turntable of T7 wind tunnel and generated using the castellated barrier (high setting) in Fig. 5(f) for Irwin probes testing.

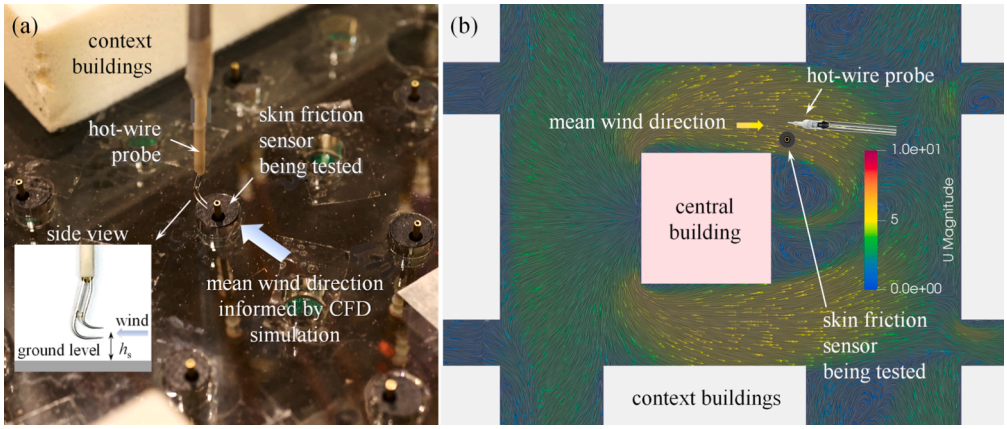

Fig. 10. Illustration of the alignment of a right-angled hot-wire probe near the surface wind sensor to be tested based on the local mean flow direction (informed by CFD simulation) at the pedestrian-level height in (a) 3D view and (b) plan view.

different surface wind sensor locations, and measurements of simultaneous ground level velocity and differential pressure are taken one at a time. Depending on the measurement location and the wind direction, the hot-wire probe's orientation is adjusted so that its prongs are always positioned downstream of the local mean velocity field near the surface wind sensor, as demonstrated in Fig. 10 (b). The latter velocity field is established numerically for the considered three wind directions using Reynolds-Averaged Navier Stokes (RANS) simulations of the AIJ case D benchmark model, using a validated digital twin of the T7 wind tunnel with realistic/measured inflow boundary conditions. This probe orientation ensures that the aerodynamic perturbations created by the probe's prongs are minimised.

To evaluate the effectiveness of the proposed calibration method, simultaneous measurements are taken at 9 specific probe locations as labelled in Fig. 8(b). These measurements are carried out for three different wind directions, 0°, 22.5°, and 45° as depicted in Fig. 8(a), at each probe location and for four distinct mean flow velocities at the central building heights, $U_m(h_{CB})$ = 4.95, 6.65, 8.35, and 10.05 m/s. In total, 108 measurement pairs are taken from 9 probe locations, 3 wind directions, and 4 mean flow velocities. This approach covers a wide range of testing flow conditions and includes low-velocity and high-turbulence regions in the AIJ case D model, such as locations 7, 16, and 18 (see Fig. 8(b)).

5. Accuracy assessment of sensor calibration

5.1. Influence of Taylor series terms in the physics-based calibration model

In this section two different calibration approaches are examined utilising the experimental data described in Sections 4.2 and 4.3 for calibration and testing purposes, respectively. The first approach applies the calibration equations, i.e., Eqs. (14) and (15), proposed by Irwin [19], while the second approach utilises Eqs. (11) and (12) proposed by the current study. The purpose of this comparison is to evaluate the influence of certain higher-order polynomial terms of the fluctuating component of the differential pressure, $\Delta p'$, on the sensor accuracy. For simplicity, the experimental data from the flat-plate setup with different barrier settings detailed in Section 4.2 will be referred to as the training set hereafter, while the data from the benchmark urban model of AIJ case D with various wind directions and mean inflow speeds will be referred to as the testing set. In the next section, the potential of coupling the proposed physics-based models, specifically Eqs. (11) and (12), with a data-driven GRNN (as detailed in Section 3) will be further explored to enhance sensor accuracy in capturing building-induced turbulence.

Starting with the Irwin's calibration models, Eqs. (14) and (15) are fitted to the training sets of mean wind speeds and speed SDs as shown in Fig. 11 (a) and (b), respectively. For this purpose, Eq. (15) is augmented with an artificial disturbance variable, similar to the treatment of Eq. (21). As seen in Fig. 11 (a), the fitted calibration model, Eq. (14), can

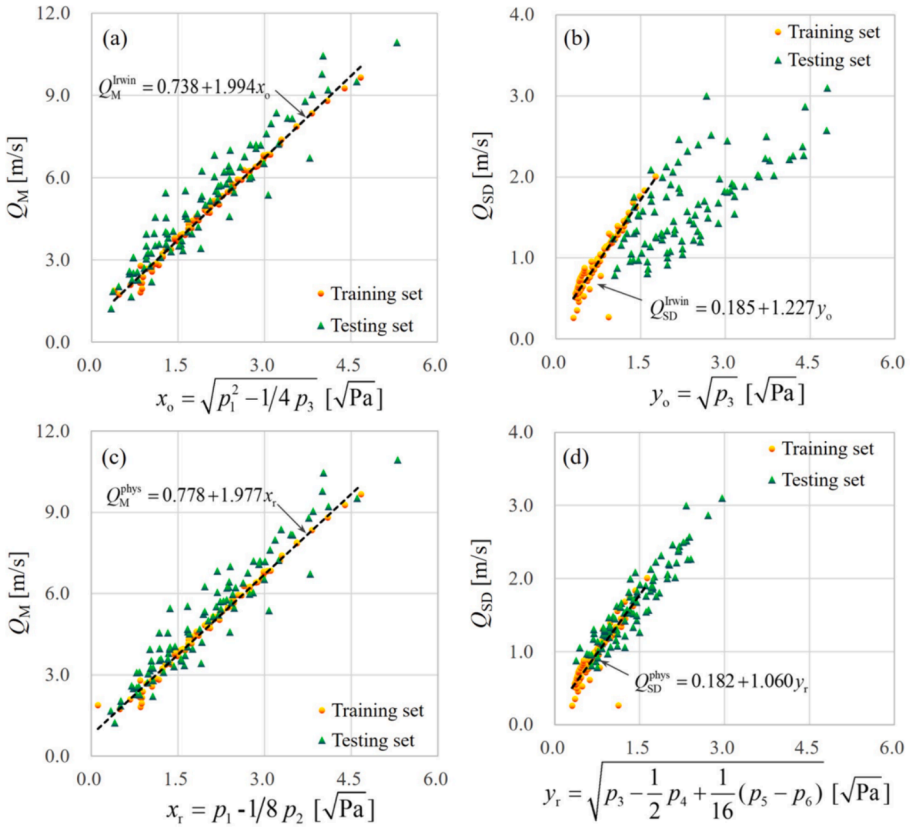

Fig. 11. Linear regression of the Irwin's models (upper row) and revised physics-based models (lower row) to the training dataset in Section 4.2 for mean wind speed (left column) and speed standard deviation (right column) predictions for the testing dataset in Section 4.3.

well capture the linear relationship between the input and response variables in the testing set of the mean wind speed Q_M, i.e., x_o and Q_M (where $x_o = \sqrt{p_1^2 - 1/4p_3}$), with a mean absolute percentage error (MAPE) of 13.2. Here, MAPE is defined as MAPE $= 1/n\sum_{i=1}^{n}|(A_i - F_i)/F_i|$, with A_i and F_i representing the actual and forecast values, respectively. However, the same is not true for the speed SD, Q_{SD}, as demonstrated in Fig. 11 (b). The Irwin calibration model, Eq. (15), can only approximate Q_{SD} in the training set but not well predict Q_{SD} in the testing set. For most of the data points in the testing set, using Eq. (15) results in significantly higher readings of Q_{SD} and TI at the pedestrian level, an issue that has been previously flagged in the literature [21].

Turning attention to the approach proposed by the current study, fitting the revised model, Eq. (12), to the training set can lead to much more accurate predictions of Q_{SD} for the testing set, as shown by the significant reduction of MAPE from 92.3 % in Fig. 11 (b) to 11.9 % in Fig. 11 (d). Therefore, if the time-averaged terms of all three higher-order polynomials of Δp' from the truncated Taylor expansion in Eq. (12) are kept for calibration, a sensor calibrated under idealised turbulent flows on a flat plate is capable of accurately predicting Q_{SD} in an urban model where building-induced turbulence exists. While this is a significant improvement, it is worth noting that using the revised calibration model for Q_M (Eq. (11)) only leads to a minor improvement in the measurement accuracy for the testing set. Indeed, by cross-comparing Fig. 11 (a) and (c), it can be seen that MAPE is only reduced slightly from 13.2 % to 11.7 %. It is worth noting that the training sets for both Q_M and Q_{SD} shown in Fig. 11 are generated using the same flat-plate setup but with different barrier settings as detailed in Section 4.2. However, an interesting observation can be made from Fig. 11: regardless of the calibration model used, all the training data points appear to form a straight line between the response variables (Q_M or Q_{SD}) and the corresponding input variables. This finding suggests that the sensor can be effectively calibrated under a single turbulent flow condition with varying mean flow speeds. Thus, there is no need to manipulate the TI levels during the sensor calibration process.

At this juncture, it is necessary to reflect that Eqs. (14) and (15) proposed by Irwin [19] are based on two assumptions: first, only the first 3 terms in the Taylor expansion are considered; and second, the time-averaged, higher-order polynomials of Δp' (than the order of 2, also see p_4, p_5, and p_6 in Eq. (13)) are neglected, due to their relatively small contributions to Q_M and Q_{SD} on a flat surface. Nevertheless, as demonstrated here, in the cases where there are building models causing high TI at h_s, the mean and SD values of the differential pressure (represented as $\overline{\Delta p}$ and $\sqrt{\overline{(\Delta p')^2}}$) can reach comparable magnitudes. As a result, the effects of these high-order polynomials can no longer be neglected for the calibration of the sensor. Under this condition, the second simplification above can cause higher turbulence/Q_{SD} "readings" from the surface wind sensor, which is consistent with the finding by Wu and Stathopoulos [21]. The herein reported results evidence that the over-prediction of Q_{SD} is due to neglecting the three higher-degree polynomials of Δp' in Eq. (13), rather than truncating the higher-order Taylor expansion terms above the 3rd order as has been conjectured by Wu and Stathopoulos [21].

5.2. *Training, feature selection, and validation of the PGNN calibration models*

In this section, two independent PGNNs (see Section 3) are trained and validated to predict Q_M and Q_{SD} using the experimental data from the flat plate test discussed in Section 4.2. To achieve this, the following optimization problem is formulated

$$\boldsymbol{x}^{*} = \min_{\boldsymbol{x}} \left[\sum_{i=1}^{n} \frac{\left| Q^{\mathrm{PGNN}}(\boldsymbol{p}_i, \boldsymbol{x}) - Q_i \right|}{Q_i} \right] \text{ subject to } \boldsymbol{x}^{\min} \leqslant \boldsymbol{x} \leqslant \boldsymbol{x}^{\max}, \tag{22}$$

to determine the hyperparameters of the proposed PGNNs. This formulation gathers the learnable parameters in vector $\mathbf{x}$, with the boundaries set by $\mathbf{x}^{\min}$ and $\mathbf{x}^{\max}$. The chosen loss function to minimise is the MAPE of all n predictions, which provides an intuitive interpretation in terms of relative error. For Q_{M} prediction, $\mathbf{x}$ is defined as [γ_{M}, α_{M}, β_{M}, σ_{M1},.., $\sigma_{\mathrm{M}m}$] (see Eq. (20)), while for Q_{SD}, $\mathbf{x}$ is defined as [γ_{SD}, $\varepsilon_{\mathrm{SD}}$, β_{SD}, $\sigma_{\mathrm{SD}1}$,.., $\sigma_{\mathrm{SD}l}$] (see Eq. (21)). In both cases, the lower bounds for all entries in $\mathbf{x}$ are set to 0. The upper search ranges for $\mathbf{x}$ are unbounded, except for the first entry (the weighting factor γ), which is bounded by 1.0. The optimal value of $\mathbf{x}$ is denoted as $\mathbf{x}^*$ in Eq. (22) and is found by minimising the loss function (MAPE) until the change in the function's value between two successive iterative steps becomes smaller than the specified tolerance of 1E-04.

To solve the optimization problem in Eq.(22), the computation of $Q^{\mathrm{PGNN}}(\mathbf{p}_i,\mathbf{x})$ ($i = 1, \ldots, n$) is performed using Eqs. (20) and (21) for Q_{M} and Q_{SD} estimates, respectively. Since the above optimisation problem is non-convex, the hyperparameters of the PGNNs are determined using a cascade optimisation process. This process begins with initial training using the Augmented Lagrangian Genetic Algorithm (ALGA) [44], followed by subsequent training using the Interior-Point Method (IPM) [45]. As a stochastic global optimisation algorithm, the use of ALGA reduces the risk of the training process getting trapped in local minima, while the subsequent use of the gradient-based IPM helps eliminate near-optimal solutions.

Before training the PGNNs, feature selection is performed for the GRNN component of the corresponding PGNN (see Fig. 2) to reduce the model's complexity and improve its interpretability and generalisability. To achieve this, the initial input vectors, after z-score standardisation, used by the adaptive GRNNs are defined in the following two equations

$$\widetilde{\boldsymbol{p}}_{\mathrm{M}} = \left[\widetilde{p}_1, \widetilde{p}_2, \widetilde{p}_7, \widetilde{p}_8\right] \text{ and } \widetilde{\boldsymbol{p}}_{\mathrm{SD}} = \left[\widetilde{p}_3, \widetilde{p}_4, \widetilde{p}_5, \widetilde{p}_6, \widetilde{p}_7, \widetilde{p}_8\right] \tag{23}$$

for Q_{M} and Q_{SD} predictions, respectively. In the last equation, $\widetilde{p}_1$ to $\widetilde{p}_6$ are defined in Eq.(21), while $\widetilde{p}_7$ and $\widetilde{p}_8$ denote the standardised mean and SD of Δp, respectively. In this setting, the first two and four entries of $\widetilde{\boldsymbol{p}}_{\mathrm{M}}$ and $\widetilde{\boldsymbol{p}}_{\mathrm{SD}}$ correspond to the physics-based input features derived from Eqs. (11) and (12) respectively, which are coming from the Taylor expansion of instantaneous $\boldsymbol{Q}(\Delta p)$. Conversely, the last two entries of $\widetilde{\boldsymbol{p}}_{\mathrm{M}}$ and $\widetilde{\boldsymbol{p}}_{\mathrm{SD}}$ represent two added statistical features of Δp(t) and do not contain any prior domain knowledge from the physics-based models. Upon optimisation, the input features in the last equation are automatically ranked by their relative importance, determined by their corresponding bandwidths $\boldsymbol{\sigma}$. In the adaptive GRNN, an input feature with a small optimised σ will have a greater impact on the calculation of the reduced Mahalanobis distance, while a feature with a relatively large optimised σ will have a minimal or even negligible impact. This intrinsic property of the adaptive GRNN enables automated feature selection by discarding features with comparatively large σ values. The selection of input features involves eliminating all the features from the standardised $\widetilde{\boldsymbol{p}}_{\mathrm{M}}$ and $\widetilde{\boldsymbol{p}}_{\mathrm{SD}}$ whose σ exceeds a given threshold. Table 1 provides a statistical summary of the input features in Eq. (23) in the full dataset, which includes both the training and testing sets from Sections 4.2 and 4.3.

At this point, two separate GRNN models are trained using the respective full training set in Section 4.1, by minimising the loss function defined in Eq. (22). Each model is trained using the same cascade optimisation approach and the same dataset for 400 times, which are sufficiently large enough for statistical convergence of optimised $\boldsymbol{\sigma}$. Fig. 12 (a) and (b) depict the median and mean values of the optimised $\boldsymbol{\sigma}$ for 4 features in $\widetilde{\boldsymbol{p}}_{\mathrm{M}}$ and 6 features in $\widetilde{\boldsymbol{p}}_{\mathrm{SD}}$, respectively. As seen in Fig. 12 (a), the most important features for Q_{M} approximation (using the adaptive GRNN) are the same two Taylor expansion terms employed in Eq. (11). This is because the median and mean values of their optimised $\boldsymbol{\sigma}$ are much smaller than those of the two added features, namely $\overline{\Delta p}$ and $\sqrt{\overline{(\Delta p')^2}}$. For Q_{SD} approximation, it is clear in Fig. 12 (b) that there are three input features, two from the Taylor expansion in Eq. (12) and one added feature $\sqrt{\overline{(\Delta p')^2}}$, that hold greater importance compared to the remaining three features.

To this end, the selected input features for the proposed PGNNs in Eqs. (19) and (20) for Q_{M} and Q_{SD} measurements, $\boldsymbol{p}_{\mathrm{M}}^{\mathrm{PGNN}}$ and $\boldsymbol{p}_{\mathrm{SD}}^{\mathrm{PGNN}}$, are presented below, reflecting the elimination of the input features with comparatively large σ value as demonstrated in Fig. 12.

$$\boldsymbol{p}_{\mathrm{M}}^{\mathrm{PGNN}} = \left[p_1, p_2, \widetilde{p}_7, \widetilde{p}_8\right] \text{ and } \boldsymbol{p}_{\mathrm{SD}}^{\mathrm{PGNN}} = \left[p_3, p_4, p_5, p_6, \widetilde{p}_3, \widetilde{p}_4, \widetilde{p}_8\right] \tag{24}$$

In this setting, the proposed PGNNs in Eq. (20) for Q_{M} measurement incorporates 4 input features in total, including two Taylor expansion-based ones from Eq. (11) for the physics-based model, as well as two standardised features in Eq. (24) for the adaptive GRNN. On the other hand, the PGNN in Eq. (21) for Q_{SD} measurement utilises 7 input features in total, consisting of four Taylor expansion-based ones from Eq. (12) for the physics-based model and three standardised features in Eq. (24) for the adaptive GRNN.

To validate the proposed PGNN, a "cross-validation" is employed, involving three different predictive models: the physics-based predictive model (Eqs. (11) or (12)), the pure adaptive GRNN (Eq. (19)), and the proposed PGNN (Eqs. (20) or (21)). These three models are trained on the same dataset generated from the flat-plate experiment detailed in Section 4.2. For validation purposes, a standard 5-fold cross-validation method is implemented to randomly split the available training data (70 in total) into 4 training folds and 1 validation fold of equal sizes. The calibration coefficients of the physics-based models are determined using linear regression, while the adaptive GRNNs and PGNNs are trained using the cascade optimisation process discussed previously. Conveniently, the pure data-driven GRNN model can be retrieved from the corresponding PGNN by setting the corresponding weighting coefficient γ in Figs. 2 to 0. In this setting, each model undergoes five rounds of training and validation. The averaged performance metrics resulted from these trainings and validations are summarised in Table 2, which includes the min and max PE, MAPE, and coefficient of determination

Table 1
Statistical description of different input features of the full dataset including the range, mean, median, standard deviation (SD), and coefficient of variation (COV) values.

	Input feature	Unit	Range	Mean	Median	SD	COV
From Taylor expansions (for physics-based models in Eqs. (11) and (12))	p_1	$\sqrt{P}$	[0.392, 5.407]	2.241	2.112	0.998	0.445
	p_2		[0.053, 5.747]	1.631	1.032	1.499	0.919
	p_3	Pa	[0.097, 23.106]	3.855	2.037	4.765	1.236
	p_4		[-0.002, 41.952]	6.380	1.592	8.613	1.350
	p_5		[0.008, 159.158]	18.504	4.422	25.486	1.377
	p_6		[0.003, 33.025]	4.895	1.065	6.830	1.395
Added	p_7	Pa	[0.154, 29.241]	6.013	4.462	5.170	0.860
(for GRNNs in Eq. (19))	p_8	$\sqrt{P}$	[0.269, 21.236]	4.103	2.669	4.104	1.000

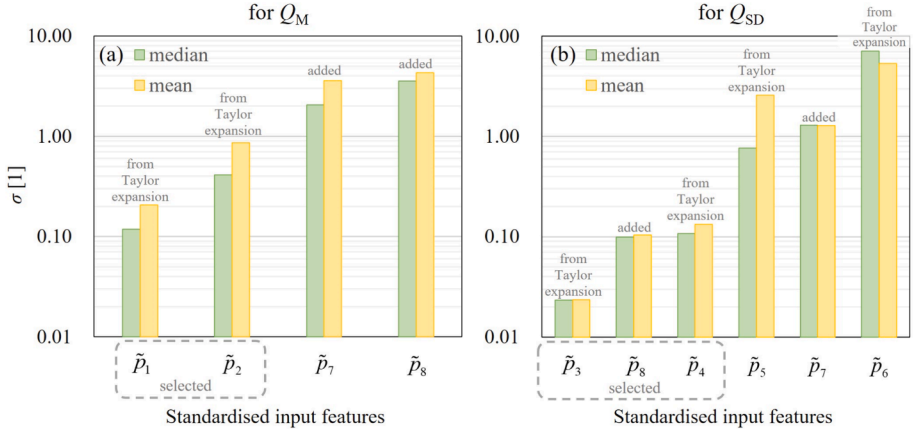

Fig. 12. Median and mean values of the optimised σ for input features in Eq. (23) using the adaptive GRNN for (a) mean wind speed and (b) speed standard deviation approximations. The values are obtained by retraining the adaptive GRNN using the full training set 400 times.

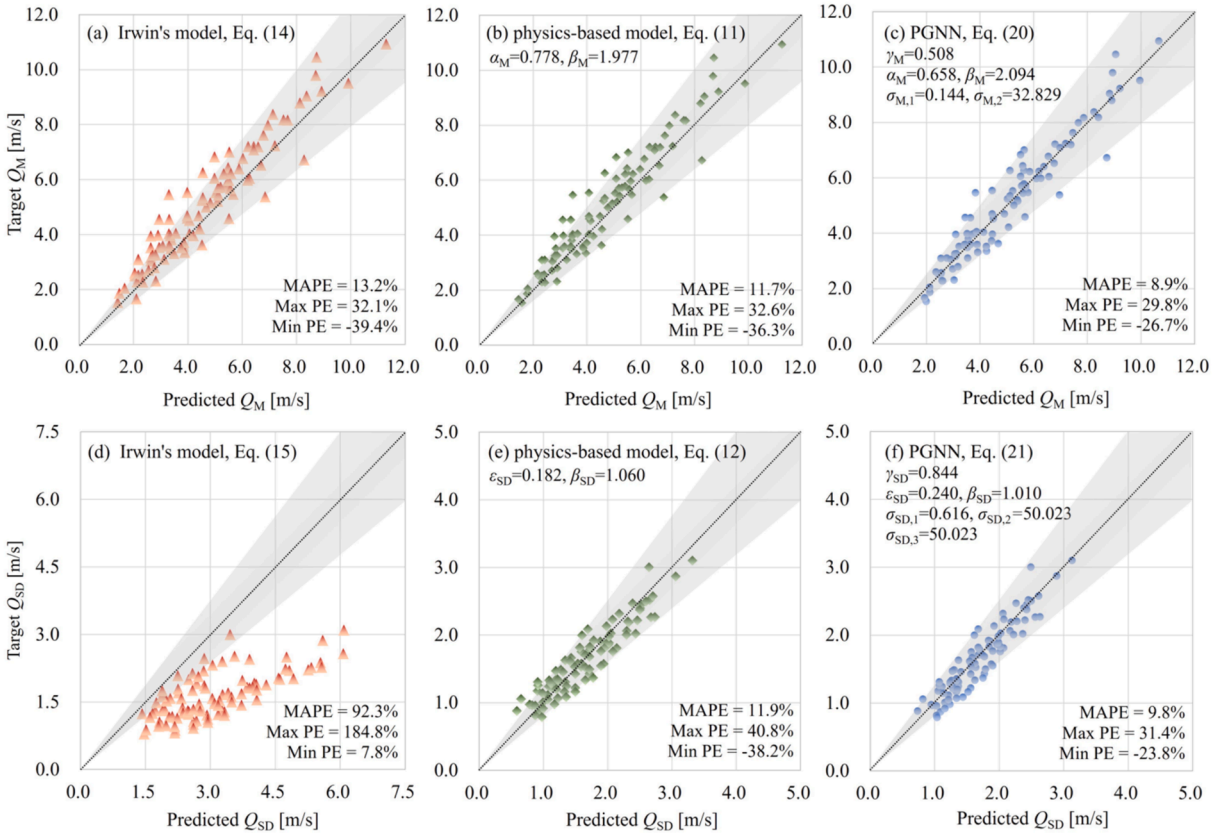

Fig. 13. Target vs. predicted mean wind speeds (upper row) and speed standard deviations (lower row) with a ± 20 % error bound (shown as the grey area) by Irwin's predictive models (left column), revised physics-based model (middle column), and physics-guided GRNN (right column).

(denoted R^2) for both Q_M and Q_{SD} estimates. Further, these performance metrics are evaluated separately across the training, validation, and full datasets.

It can be observed from Table 2 that all three models perform generally well for approximating and predicting Q_M on the full and validation datasets, with their Q_M estimates all falling within the ± 16 % error bound. Still, the adaptive GRNN exhibits a slightly wider error bound for the training and validation datasets compared to the physics-based model and PGNN. Similar trends are also observed for Q_{SD} estimates, albeit with increased MAPEs and widened error bounds across all models in general. Nevertheless, the adaptive GRNN shows much wider error bounds for all three types of datasets, with its min and max PEs doubling from [-15.7 %, +19.0 %] for Q_M estimates to [-37.4 %, 41.9 %] for Q_{SD} estimates. Among the three models, the proposed PGNN consistently outperforms the other two for both Q_M and Q_{SD} predictions across the three datasets. However, the application of it does not result in significant improvements in the measurement accuracy of the surface wind sensors compared to the physics-based model, despite requiring slightly more training effort.

Finally, it is important to note that the proposed PGNN is found to be highly robust to overfitting. This is largely attributed to its use of limited number of DOFs, specifically 5 DOFs ([γ_M, α_M, β_M, σ_{M1}, σ_{M2}]) for Q_M predictions and 7 DOFs ([γ_{SD}, ε_{SD}, β_{SD}, σ_{SD1}, σ_{SD2}, σ_{SD3}]) for Q_{SD} predictions. Consequently, the size of the training set is an order of

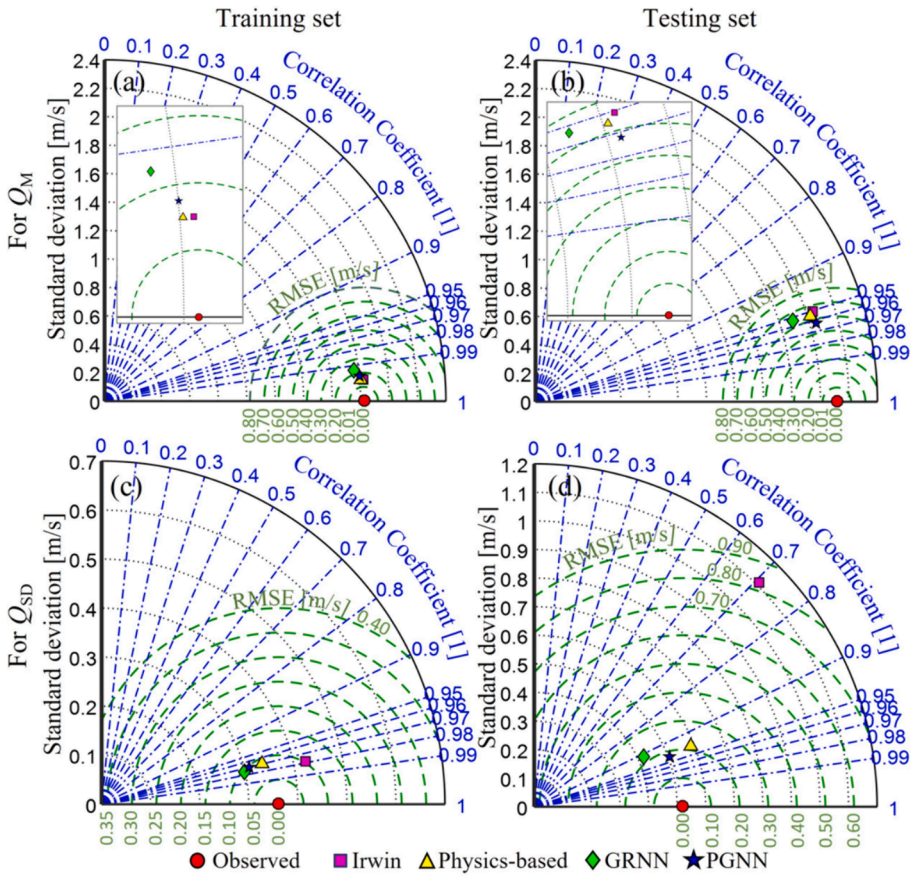

Fig. 14. Taylor diagrams of the three different predictive models in Fig. 12 for mean wind speed (upper row) and speed standard deviation (lower row) approximations/predictions considering the training (left column) and testing (right column) datasets.

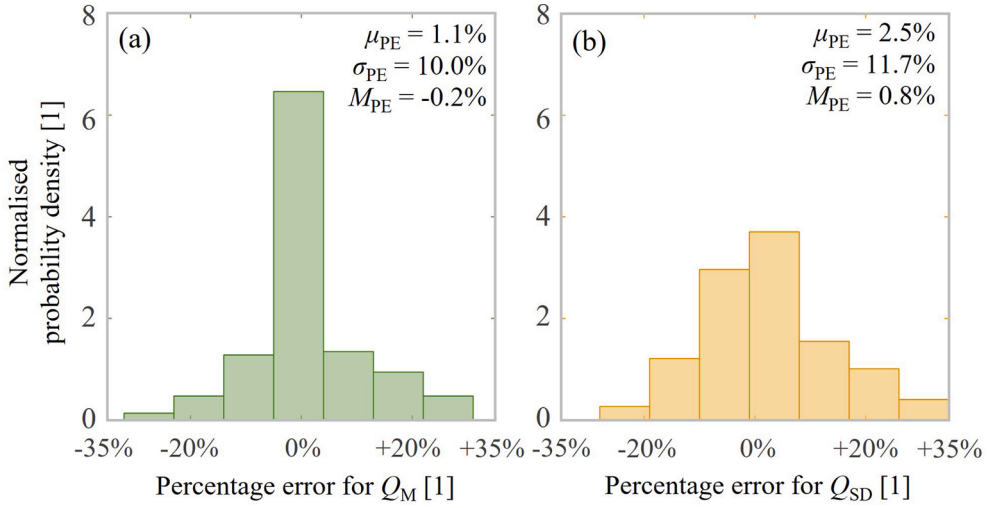

Fig. 15. Histograms of percentage errors of all (a) mean wind speed and (b) speed standard deviation predictions by the proposed physics-guided general regression neural network considering the testing dataset.

magnitude larger than the number of hyperparameters, rendering the issue of overfitting generally negligible. Conversely, the concern of underfitting is also of minimal significance in the proposed PGNNs, which is attributed to the additional DOFs introduced through the weighting operation and the utilisation of unique bandwidths for each input feature in the adaptive GRNN.

5.3. *Prediction accuracy of PGNN calibration model*

In this section, the PGNNs trained in last section are applied to predict the pedestrian-level mean wind speeds and speed SDs at 9 selected locations in the AIJ case D benchmark urban model as indicated in Fig. 8(b). The aim is to assess the generalisation performance of the proposed PGNN calibration approach for evaluating urban pedestrian-level winds in comparison to Irwin's calibration models and physics-

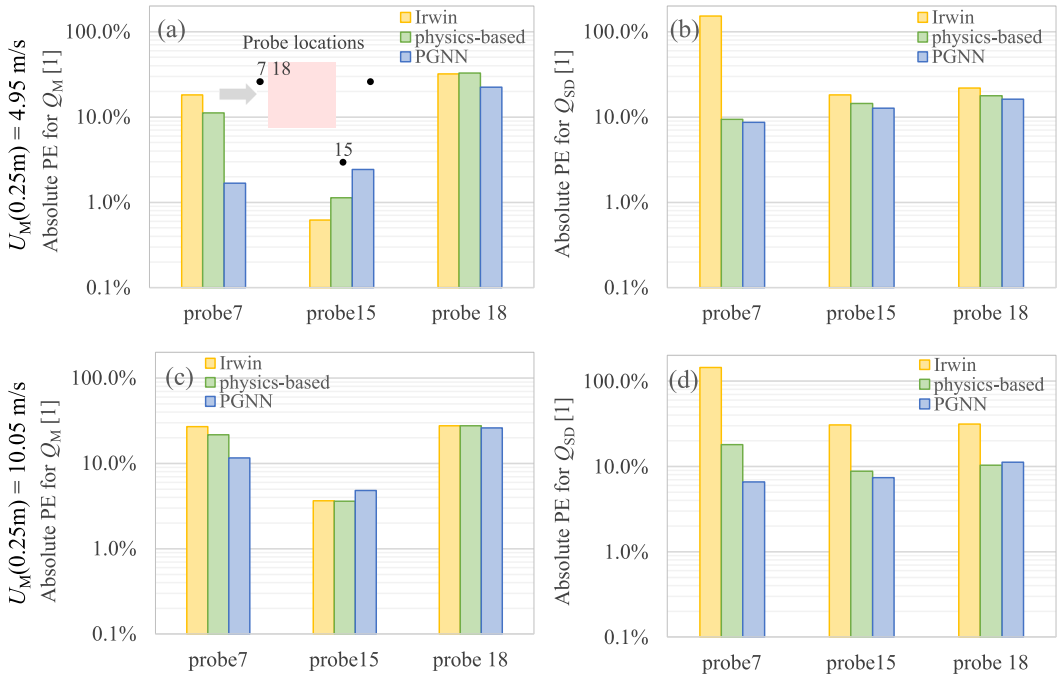

Fig. 16. Absolute percentage errors of mean wind speed (left column) and speed standard deviation (right column) predictions by the three predictive models in Fig. 13 at three critical locations around the central building model for wind direction of 0° and two inflow speeds at the central building height.

Table 2
Performance metrics of three different models.

Output	Model	Training set (approximation) min/ max PE	MAPE	R^2	Validation set (generalisation) min/ max PE	MAPE	R^2	Full set (approximation) min/ max PE	MAPE	R^2
Mean, Q_M	Physics Eq. (11)	−10.4/ +15.3 %	3.4 %	0.973	−13.5 %/ +15.3 %	3.9 %	0.971	−13.9 %/ +15.2 %	3.5 %	0.975
	GRNN Eq. (19)	−14.9/ +15.5 %	3.6 %	0.978	−15.7 %/ +19.0 %	3.7 %	0.971	−12.4 %/ +13.81 %	3.6 %	0.977
	PGNN Eq. (20)	−13.4 %/ +15.0 %	3.2 %	0.984	−13.7 %/ +15.6 %	3.3 %	0.981	−13.0 %/ +14.7 %	3.1 %	0.982
Standard deviation, Q_{SD}	Physics Eq. (12)	−14.1 %/ +23.0 %	6.3 %	0.959	−15.7 %/ +21.6 %	8.2 %	0.952	−15.3 %/ +16.0 %	6.4 %	0.958
	GRNN Eq. (19)	−30.6 %/ +33.6 %	6.6 %	0.920	−37.4 %/ +41.9 %	7.1 %	0.915	−26.5 %/ +28.3 %	5.7 %	0.940
	PGNN Eq. (21)	−14.9 %/ +15.2 %	6.3 %	0.961	−18.1 %/ +17.5 %	6.4 %	0.960	−17.0 %/ +16.1 %	5.8 %	0.963

based models that utilise higher-order polynomials of Δp'. As a remark, the training and validation datasets used in the analysis stem from the flat-plate experiment outlined in Section 4.2, devoid of any building models. The current section demonstrates that employing the proposed PGNN, trained on the flat-plate dataset, yields significant improvements in the prediction accuracy of surface wind sensors concerning MAPE, error bound, and root mean square error (RMSE) in the presence of building-induced turbulence. Cross-validated PGNNs are iteratively trained 400 times using the entire training set and the cascade optimisation method. The final PGNN models are constructed by averaging optimal hyperparameters derived from these iterations. These models are then applied to the testing dataset derived from the AIJ case D model to showcase their extrapolation capabilities in the following section. In this regard, Fig. 13 displays the measured/target versus predicted mean wind speeds and speed SDs from three models: simplified Irwin's models in Eqs. (14) and (15), herein derived models in Eqs. (11) and (12), and proposed PGNNs in Eqs. (20) and (21). The pure adaptive GRNN from the last section is excluded due to its inferior performance (in terms of error bounds for Q_{SD}) compared to the other two models. Specifically, the upper and lower rows of Fig. 13 are for mean wind speed and speed SD, Q_M and Q_{SD}, respectively, and the three columns of Fig. 13 from left to right are for simplified models in Eqs. (14) and (15), the physics-based models in Eqs. (11) and (12), and PGNNs, respectively. Each subplot includes MAPE as well as min and max PE of all predictions in the lower right corners, while the optimised calibration coefficients for the physics-based predictive models and hyperparameters for the PGNNs are displayed in the upper left corners. It can be observed from the upper row of Fig. 13 that all three models predict Q_M well with a MAPE less than 14 %. In addition, the MAPE value gradually decreases from 13.2 % for Irwin's model to 11.7 % for the physics-based model and finally to 8.9 % only for the proposed PGNN. Meanwhile, the error bound is seen to steadily narrow as well. Furthermore, most of the data points of the three models are within the ± 20 % error bound shaded in grey, and the number of outliers outside the shaded region keeps reducing as the predictive model advances to the proposed PGNN. In summary, all three models provide accurate predictions of mean wind speeds with a small scatter, and the proposed PGNN offers the best prediction performance.

Focusing on the lower row for Q_{SD} prediction, Fig. 13 (d)

demonstrates that the Irwin's calibration model results in significant overestimates of Q_{SD}, with PE and MAPE reaching as high as 184.8 % and 92.3 %, respectively. As discussed previously, this is due to the omission of the three higher-order terms of $\Delta p'$ in Eq. (13). Indeed, as seen in Fig. 13(e), including these additional terms in the model, Eq. (12), significantly improves the accuracy of Q_{SD} measurements, with the maximum PE reduced from 184.8 % to 40.8 % and MAPE from 92.3 % to 11.9 %. Also, the majority of Q_{SD} predictions are now within the ± 20 % error bound. Finally, the proposed PGNN provides even better consistency between the target and predicted Q_{SD} values, as illustrated in Fig. 13 (f), with MAPE reduced to 9.8 % and the min/max PE to −31.4 % and 23.8 %, respectively. Again, most of the Q_{SD} estimates by PGNN are within ± 20 % error bound, with a few exceptions occurring for $Q_{SD} <$ 1.5 m/s.

To provide a more thorough analysis, all four calibration models, namely the Irwin's model, physics-based model, adaptive GRNN, and proposed PGNN, are further examined using Taylor diagrams [46] as depicted in Fig. 14. The upper row of subplots illustrates Q_M approximations for the training set (left) and predictions for the testing set (right), while the lower row displays Q_{SD}. These diagrams show the correlation coefficient and SD of the approximations/predictions for each model, with the RMSE of the approximations/predictions represented by the distance from the observed point to the corresponding model symbol. In this setting, the observation point on the *x*-axis represents a perfect prediction, with zero RMSE and unit correlation coefficient, with the corresponding SD. Therefore, the location of each model symbol in the diagram indicates how closely the predictions by a model match the actual observations. Fig. 14 reveals that both Q_M and Q_{SD}, predicted by the physics-based models, GRNNs, and PGNNs, show strong correlation (over 0.95 for the training dataset and over 0.90 for the testing dataset). Additionally, these three models exhibit similar SDs as the observations, as measured by the radial distance between the centre of each circular section and the model symbol. However, the Irwin's model performs poorly in predicting Q_{SD}, as demonstrated in Fig. 14 (d), with a correlation coefficient of just above 0.7, in contrast to the other three models which have correlation coefficients above 0.9. Furthermore, the proposed PGNN model consistently outperforms the other three models in terms of the considered model performance metrics for both Q_M and Q_{SD} predictions, confirming the trends observed in the lower row of subplots in Fig. 13, albeit now using different metrics.

In Fig. 15, the histogram shows the distribution of PEs for Q_M predictions, with a mean value (denoted by μ_{PE}) of 1.1 %, SD (denoted by σ_{PE}) of 10.0 %, and median value (denoted by M_{PE}) of −0.2 %. The histogram exhibits a bell-shaped curve reminiscent of a Gaussian distribution with symmetrical error bounds about the centre, though with a narrowed "neck" region. This indicates that most of the Q_M predictions by the PGNN are concentrated in the centre with small PEs, implying a higher level of measurement accuracy. On the other hand, Fig. 14(b) shows the histogram for Q_{SD} predictions with $\mu_{PE} = 2.5$ %, $\sigma_{PE} = 11.70$ %, and $M_{PE} = 0.8$ %. The histogram for Q_{SD} predictions shows a Gaussian-like distribution, but with a slightly wider spread compared to the Q_M predictions, indicating a lower level of accuracy for Q_{SD} measurement (compared to Q_M measurement). Overall, the histograms show that the PGNNs' predictions by the proposed PGNN are unbiased for both Q_M and Q_{SD} measurements.

Finally, the accuracy of the surface wind sensor calibrated using the proposed PGNN is evaluated using wind direction 0° and two inflow velocities (at the central building height), $U_M(0.25\text{ m}) = 4.95$ and 10.05 m/s, at three critical locations around the central building model (probe locations 7, 15, and 18) in Fig. 16. Specifically, Fig. 16 (a) and (c) show the absolute PEs for Q_M measurements by the three calibration models in Fig. 13 for the low- and high-speed settings (i.e., 4.95 and 10.05 m/s), respectively, while Fig. 16 (b) and (d) show the same for Q_{SD}. These locations, which cover the front, side, and wake regions of the central building model, are demonstrated in Fig. 16 (a). As seen in Fig. 16 (a) and (c), the surface wind sensor calibrated using the proposed PGNN can predict Q_M more accurately than the Irwin's model and physics-based model for both speed settings in the front and side regions, with absolute PEs of less than 10 %. However, in the wake region, the absolute PEs of the predictions by all three models are comparable and increase to 20 %. Regarding Fig. 16 (b) and (d), all three models generally predict Q_{SD} well with absolute PEs of less than 20 % for both speed settings, except for Irwin's model, which significantly overpredicts the speed SD by 100 % in front of the building model.

6. Concluding remarks

Skin friction sensors play a crucial role in measuring the frictional stress resulting from fluid flow over solid surfaces, providing both qualitative and quantitative insights into airflow near solid bodies within boundary layers. Among these sensors, the surface wind sensor developed by Irwin [19] has found widespread adoption in wind tunnel experiments, particularly those focusing on urban and environmental aerodynamics. However, when calibrated using the current physics-based method, the accuracy of this sensor in measuring flow speed fluctuations in regions with low flow velocity and high turbulence has been a subject of concern. This study has addressed this limitation by introducing a physics-guided neural network (PGNN) calibration approach aimed at improving the accuracy of this sensor for measuring low-frequency speed fluctuations in the above condition. The proposed method integrates a refined physics-based model derived from Irwin's original calibration equations with a data-driven adaptive general regression neural network (GRNN). The results demonstrate significant improvements in measuring both mean wind speed (Q_M) and speed standard deviation (Q_{SD}). To assess the effectiveness of the proposed calibration model, different experimental setups were established in the Industrial T7 wind tunnel facility at City, University of London, generating independent datasets for training and assessing the prediction accuracy of the proposed model, separately. The calibration of the sensor was conducted on an empty flat plate under a variety of tripped turbulent boundary layer flows, while the accuracy of the sensor (calibrated using the proposed approach) was assessed at multiple critical locations within a 1:400 benchmark urban model.

The experimental results clearly demonstrate the superiority of the proposed PGNN calibration strategy over Irwin's original approach in accurately measuring both TI and mean wind speed, while maintaining strong robustness to overfitting due to the limited model complexity and number of hyperparameters involved. This advancement significantly enhances the understanding of utilising the law of the wall and data-driven model for the calibration of the sensor in three key aspects. First, it is found that using the first three Taylor expansion terms during the derivation of the physics-based calibration equations is sufficient for measuring both Q_M and Q_{SD}. For increased measurement accuracy, it is recommended to use Eqs. (11) and (12) proposed in this study for sensor calibration. Second, as long as no higher-order terms of $\Delta p'$ are neglected, the sensor calibration can be performed on an empty flat plate under idealised turbulent flow conditions with uniform roughness. This finding significantly simplifies the sensor calibration process, as the sensor can be calibrated under a single flow condition with varying mean flow speeds and subsequently used to measure non-idealised turbulent flows induced by roughness elements with sharp edges. Finally, the hybrid calibration approach, incorporating the physics-based model and adaptive GRNN, was shown to outperform each individual model (used independently) in terms of both approximation and generalisation performance. To ensure optimal performance of the proposed calibration model, the complementary weighting factors for the two constituent models were treated as hyperparameters during training. For Q_M and Q_{SD} measurements, the optimal weightings for the physics-based predictions were determined to be 0.508 and 0.844, respectively.

Overall, this study provides valuable insights into enhancing the accuracy of surface wind sensors and paves the way for more reliable flow speed measurements in wind tunnel experiments, ultimately

contributing to the development of safer and more comfortable urban environments.

CRediT authorship contribution statement

Zixiao Wang: Conceptualization, Data curation, Formal analysis, Methodology, Validation, Writing – original draft, Writing – review & editing. **Agathoklis Giaralis:** Writing – review & editing, Supervision, Project administration, Methodology, Funding acquisition, Conceptualization. **Steven Daniels:** Writing – review & editing, Supervision, Methodology, Investigation, Conceptualization. **Mingzhe He:** Writing – review & editing, Validation, Investigation. **Alessandro Margnelli:** Software, Resources, Project administration, Funding acquisition. **Chetan Jagadeesh:** Validation, Supervision, Resources, Methodology.

Declaration of competing interest

The authors declare that they have no known competing financial interests or personal relationships that could have appeared to influence the work reported in this paper.

Data availability

Data will be made available on request.

Acknowledgements

This work has been financially supported partly by Innovate UK and partly by AKT-II Ltd through the Knowledge Transfer Partnership award KTP012484. This financial support is gratefully acknowledged by all the authors.

References

[1] S. Große, W. Schroder, Mean wall-shear stress measurements using the micro-pillar shear-stress sensor MPS^3, Meas. Sci. Technol. 19 (2008) (2007) 015403.
[2] Y.A. Cengel, J.M. Cimbala, Fluid mechanics: Fundamentals and applications, (4th ed.)., McGraw-Hill Education, 2017.
[3] G. Vita, Z. Shua, M. Jessona, A. Quinna, H. Hemidaa, M. Sterlinga, C. Bakera, On the assessment of pedestrian distress in urban winds, Journal of Wind Engineering & Industrial Aerodynamics 203 (2020) (2020) 104200, https://doi.org/10.1016/j.jweia.2020.104200.
[4] Y. Zhao, R. Li, L. Feng, Y. Wu, J. Niu, N. Gao, Boundary layer wind tunnel tests of outdoor airflow field around urban buildings: A review of methods and status, Renewable and Sustainable Energy Reviews 167 (2022) 112717, https://doi.org/10.1016/j.rser.2022.112717.
[5] K.G. Winter, An outline of the techniques available for the measurement of skin friction in turbulent boundary layers, Prog. Aerospace Sci. 18 (1977) 1–57.
[6] B. Liu, J. Pang, X. Tu, Z. Zhou, Three components strain-gauge type aircraft surface friction resistance sensor: Design, manufacturing, and calibration, Measurement 218 (2023) 113165, https://doi.org/10.1016/j.measurement.2023.113165.
[7] B. Walter, C. Gromke, K. Leonard, C. Manes, M. Lehning, Spatially resolved skin friction velocity measurements using Irwin sensors: A calibration and accuracy analysis, J. Wind Eng. Ind. Aerodyn. 104–106 (2012) (2012) 314–321.
[8] A.D. Ferreira, T. Thiis, N.A. Freire, A.M.C. Ferreira, A wind tunnel and numerical study on the surface friction distribution on a flat roof with solar panels, Eviron. Fluid Mech. 19 (2019), https://doi.org/10.1007/s10652-018-9641-5.
[9] J.D. Ackerman, T.M. Hoover, Measurement of local bed shear stress in streams using a Preston-static tube, Limnology and Oceanography 46 (8) (2001) 2080–2087.
[10] J.H. Preston, The determination of turbulent skin friction by means of Pitot tubes, The Aeronautical Journal 58 (518) (1954) 109–121.
[11] F. Hirt, H. Thomann, Measurements of wall shear stress in turbulent boundary layers subject to strong pressure gradients, J. Fluid Mech. 171 (1986) 547–562.
[12] L. Tanner, L. Blows, A study on the motion of oil films on surfaces in air flow, with application to the measurement of skin friction, J. Phys. e: Sci. Instrum. 9 (1976) 194–202.
[13] M.A. Schmidt, R.T. Howe, S.D. Senturia, J.H. Haritonidis, Design and calibration of a microfabricated floating-element shear-stress sensor, IEEE Trans. Electron Devices 35 (1988) 750–757.
[14] N. Kasagi, R.J. Moffat, M. Hirata, Liquid crystals, in: R.J. Moffat (Ed.), Handbook of Flow Visualization, Hemisphere, 1989, pp. 105–123.
[15] A.V. Boiko, V.I. Kornilov, Hot-wire anemometer measurement of local skin friction coefficient, Thermophysics and Aeromechanics 17 (4) (2010) 577–586.
[16] H.H. Fernholz, G. Janke, M. Schober, P.M. Wagner, D. Warnack, New developments and applications of skin-friction measuring techniques, Meas. Sci. Technol. 7 (1996) 1396–1409.
[17] L. Lofdahl, M. Gad-el-Hak, MEMS-based pressure and shear stress sensors for turbulent flows, Meas. Sci. Technol. 10 (1999) 665–686.
[18] J. Naughton, M. Sheplak, Modern developments in shear-stress measurement, Prog. Aerosp. Sci. 38 (2002) 515–570.
[19] H.P.A.H. Irwin, A simple omnidirectional sensor for wind-tunnel studies of pedestrian-level winds, Journal of Wind Engineering and Industrial Aerodynamics 7 (1981) (1981) 219–239.
[20] F.H. Durgin, Pedestrian level wind studies at the Wright brothers facility, Journal of Wind Engineering and Industrial Aerodynamics 44 (1992) 2253–2264.
[21] H.Q. Wu, T. Stathopoulos, Further experiments on Irwin's surface wind sensor, Journal of Wind Engineering and Industrial Aerodynamics 53 (1994) (1994) 441–452.
[22] D.M. Crawley, W.G. Nickling, Drag partition for regularly-arrayed rough surfaces, Boundary-Layer Meteorology 107 (2003) 445–468.
[23] B. Walter, C. Gromke, K. Leonard, C. Manes, M. Lehning, Spatial-temporal surface shear-stress variability in live plant canopies and cube arrays, Boundary-Layer Meteorology (2011), https://doi.org/10.1007/s10546-011-9690-5.
[24] B. Blocken, T. Stathopoulos, J.P.A.J. Van Beeck, Pedestrian-level wind conditions around buildings: Review of wind-tunnel and CFD techniques and their accuracy for wind comfort assessment, Building and Environment 100 (2016) (2016) 50–81.
[25] N. Isymov, A.G. Davenport, The Ground Level Wind Environment in Built up Areas, Cambridge University Press, 1975.
[26] A.A. Townsend, Equilibrium layers and wall turbulence, J. Fluid Mech. 11 (1961) (1961) 97–120.
[27] B. Blocken, W.D. Janssen, T. Hooff, CFD simulation for pedestrian wind comfort and wind safety in urban areas: General decision framework and case study for the Eindhoven University campus, Environmental Modelling & Software. 30 (2012) 15–34.
[28] P.M. Handford, P. Bradshaw, The pulsed-wire anemometer, Exp. Fluids 7 (1989) 125–132.
[29] D.W. Bechert, On the calibration of Preston tubes, AIAA J. 34 (1995) 205–206.
[30] R. Semaan, Optimal sensor placement using machine learning, Computers and Fluids 159 (2017) (2017) 167–176.
[31] J. Giehler, L. Chamard, C. Ebert, J. Weiss, A. Giani, P. Combette, Surrogate-based parameter exploration for the design of MEMS calorimetric wall shear stress sensors by means of CFD, Sensors & Actuators: a. Physical 347 (2022) (2022) 113949.
[32] S.A. Khan, D.T. Shahani, A.K. Agarwala, Sensor calibration and compensation using artificial neural network, ISA Transactions 42 (2003) (2003) 337–352.
[33] S.L. Brunton, J.N. Kutz, Data-Driven Science and Engineering Machine Learning: Dynamical Systems, and Control, (2nd ed.), Cambridge University Press, 2021.
[34] D.F. Specht, H. Romsdahl, Experience with adaptive probabilistic neural networks and adaptive general regression neural networks, Proceedings of the IEEE World Congress on Computational Intelligence 2 (1994) 1203–1208.
[35] D.F. Specht, A general regression neural network, IEEE Transactions on Neural Networks 2 (6) (1991) 568–576.
[36] S. Robert, L. Foresti, M. Kanevski, Spatial prediction of monthly wind speeds in complex terrain with adaptive general regression neural networks, Int. J. Climatol. 33 (2013) 1793–1804.
[37] F.M. White, Fluid Mechanics, 4th ed, McGraw-Hill, New York, 1999.
[38] E. Parzen, On estimation of a probability density function and mode, The Annals of Mathematical Statistics 33 (3) (1962) 1065–1076.
[39] M. Rosenblatt, Remarks on some nonparametric estimates of a density function, Annals of Mathematical Statistics 27 (1956) 832–837.
[40] M. Rosenblatt, Curve estimates, The Annals of Mathematical Statistics 42 (6) (1970) 1815–1842.
[41] D.M. Sykes, A new wind tunnel for industrial aerodynamics, Journal of Industrial Aerodynamics 2 (1977) (1977) 65–78.
[42] SurreySensors Ltd. 2020. 64-Channel Pressure Scanner System User Manual. Guildford, Surrey: SurreySensor Ltd. Retrieved April 30, 2023, from https://www.surreysensors.com/wp-content/uploads/2021/05/USM-DPS14-042020-2.2.pdf.
[43] DanTec Dynamics Ltd, MiniCTA and Multichannel CTA Compact CTA Systems for accurate flow investigations, Retrieved April 30, 2023, from, https://www.dantecdynamics.com/wp-content/uploads/2020/03/0560_v1-1_SS-MiniCTA-Multichannel-CTA-systems.pdf, 2020.
[44] A.R. Conn, N.I.M. Gould, P.L. Toint, A Globally Convergent Augmented Lagrangian Algorithm for Optimization with General Constraints and Simple Bounds, SIAM Journal on Numerical Analysis 28 (2) (1991) 545–572.
[45] R.H. Byrd, M.E. Hribar, J. Nocedal, An Interior Point Algorithm for Large-Scale Nonlinear Programming, SIAM J Optim 9 (1999) 877–900, https://doi.org/10.1137/S1052623497325107.
[46] K.E. Taylor, Summarizing multiple aspects of model performance in a single diagram, J Geophys Res: Atmos 106 (D7) (2001) 7183–7192.